

## Research paper

# Pore characterization and shale facies analysis of the Ordovician-Silurian transition of northern Guizhou, South China: The controls of shale facies on pore distribution

Yifan Li<sup>a,b,\*</sup>, Juergen Schieber<sup>c</sup>, Tailiang Fan<sup>a,b</sup>, Xiaojie Wei<sup>d,\*\*</sup>

<sup>a</sup> School of Energy Resources, China University of Geosciences (Beijing), Beijing, 100083, China

<sup>b</sup> Key Laboratory of Strategy Evaluation for Shale Gas, Ministry of Land and Resources, China University of Geosciences (Beijing), Beijing, 100083, China

<sup>c</sup> Department of Geological Sciences, Indiana University, Bloomington, IN, 47403, United States

<sup>d</sup> Institute of Geomechanics, Chinese Academy of Geological Sciences, 100081, Beijing, China

## ARTICLE INFO

**Keywords:**

Yangtze Platform  
Wufeng-Longmaxi succession  
Black shales  
Shale gas  
Porosity  
Scanning electron microscopy

## ABSTRACT

The Ordovician-Silurian Wufeng-Longmaxi Formations in the Upper Yangtze Platform have been considered as the most promising shale play in China. However, few studies of detailed shale facies and their influence on pore distribution have been conducted. Therefore, it is important to describe the heterogeneity of shale facies in detail and elucidate their relationship to pore networks and development. Seven distinct facies were identified on the basis of their characteristic physical, biological, and chemical attributes. Ion-milled samples from all facies were examined with SEM for identification of pore types. Point-counting was used to quantify porosity. Four major pore types appear dominant: framework pores, phyllosilicate framework (PF) pores, intrapores within inorganic grains, and organic matter (OM) pores. Due to variability in composition and depositional setting of the different facies, pore networks are not uniform. Framework pores between detrital grains and PF pores are widespread in bioturbated claystones. Pores in black siliceous shales are dominated by framework pores supported by authigenic silica. Most of these are filled with kerogen/bitumen that is host to "foam" and "bubble" type OM pores. Intrapores within calcite or dolomite grains are common in fossiliferous mudstones and black dolomitic siltstones, but are isolated and do not contribute to productive porosity. In muddy siltstones, PF pores are well developed within silty bands. Initial framework pores within silty beds or laminae, however, were subsequently cemented by calcite or destroyed by compaction. As most of primary PF pores and primary frameworks pores are lost during compaction, porosity is highly dependent on the population of framework pores between authigenic quartz grains. Secondary cracking of amorphous organic matter added porosity after initial infilling of porosity by oil and bitumen migration. Therefore, porosity is mainly controlled by abundance of authigenic silica and TOC, in spite of differences of burial diagenesis among various facies. Understanding these main controls on porosity should be helpful to predict and find more porous facies and have a significant impact on future gas exploration in the Wufeng-Longmaxi Formations.

## 1. Introduction

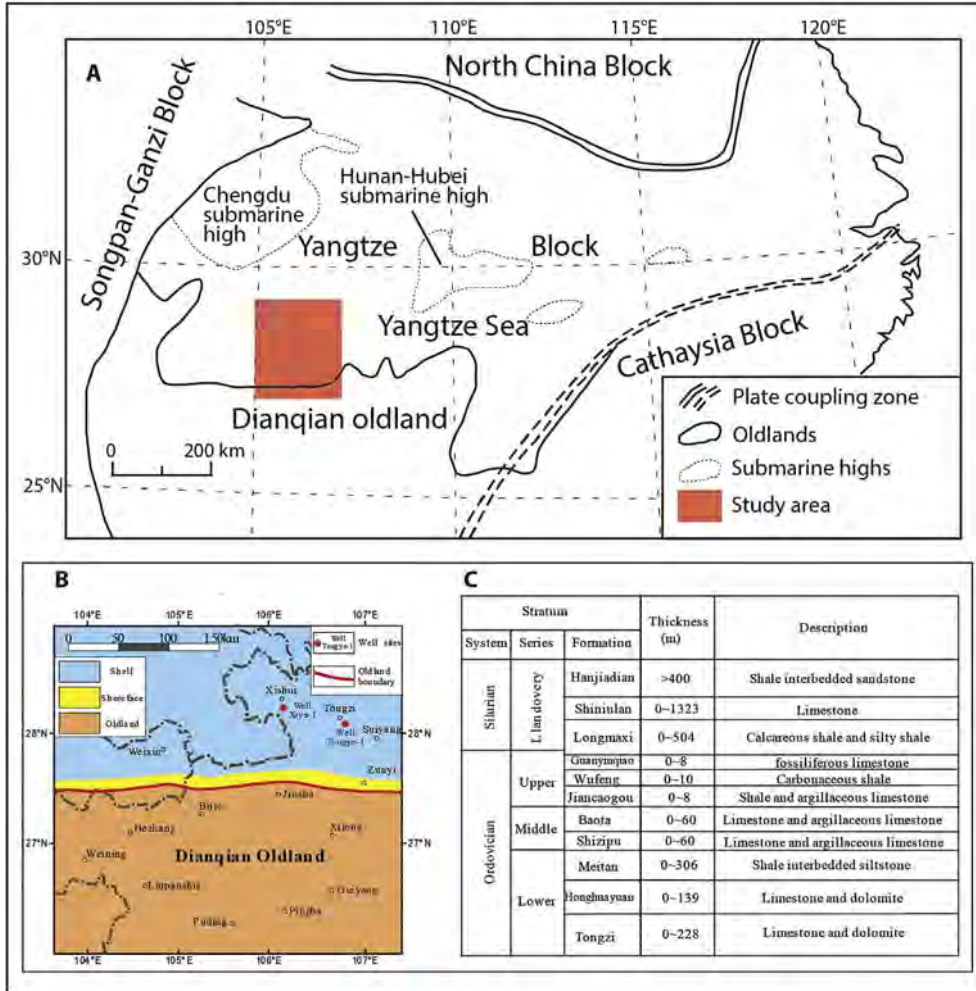
In low-permeability shales, interconnected nanometer to micrometer scale pores are the basis for gas flow in shale formations, and are critical to productivity of unconventional shale gas reservoirs (Afsharpoor and Javadpour, 2016; Curtis et al., 2010; Javadpour, 2009). During the last decade, research has been widely conducted to describe and identify a variety of pore types in many shale successions (e.g. Curtis et al., 2010; Desbois et al., 2009; Loucks et al., 2012; Milner et al., 2010; Passey et al., 2010; Schieber, 2013; Slatt and O'Brien,

2011). In addition, fractal dimension has also been used to decipher and quantify the irregularity of pores structures in shale matrix (Tang et al., 2015; Yang et al., 2014). Shales have been shown as the product of a range of processes and are inherently heterogeneous at variable scales (Guy Plint and Baas, 2014; Harazim and McIlroy, 2015; Lazar et al., 2015; Macquaker et al., 2007; Schieber, 1999; Wilson and Schieber, 2014, 2015). The heterogeneity of sedimentological attributes (texture, composition and bedding) has influence on the type, abundance, and distribution of pores (Ko et al., 2017; Schieber et al., 2016; Wilson and Schieber, 2016). Within a sequence stratigraphic framework, facies and

\* Corresponding author. School of Energy Resources, China University of Geosciences (Beijing), Beijing, 100083, China.

\*\* Corresponding author.

E-mail addresses: [yifangeosci@gmail.com](mailto:yifangeosci@gmail.com) (Y. Li), [vivi-stefanie2008@hotmail.com](mailto:vivi-stefanie2008@hotmail.com) (X. Wei).



associated porosity characteristics vary systematically (Schieber et al., 2016; Wilson and Schieber, 2016) and have important implications for reservoir performance.

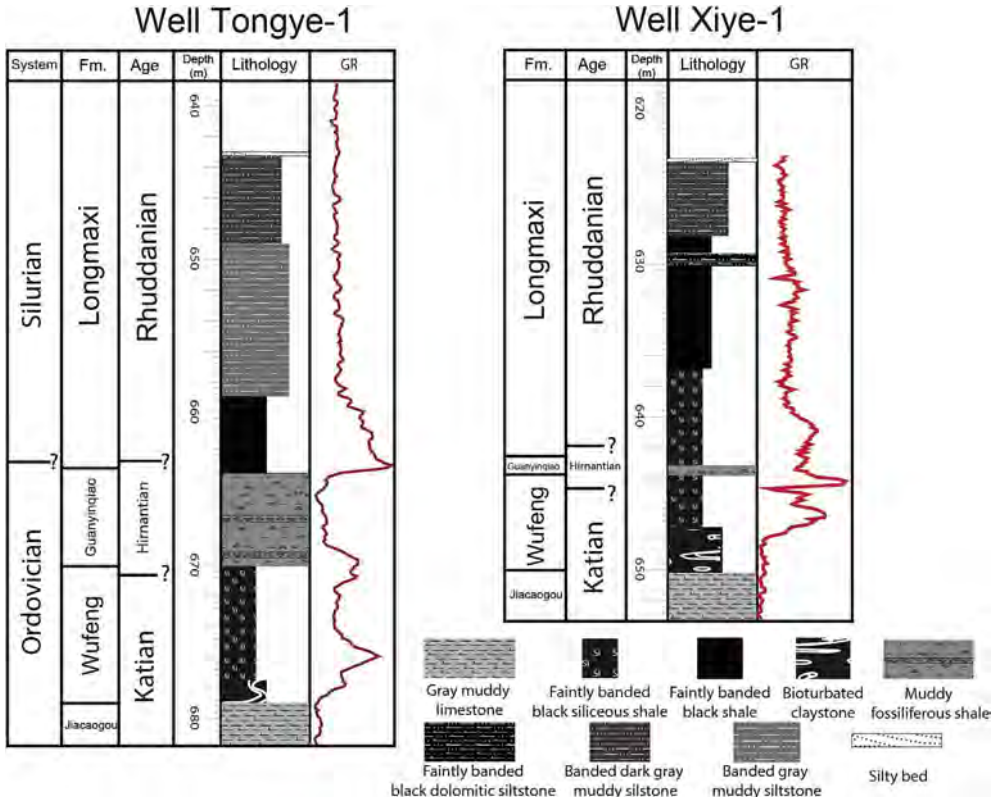
The upper Ordovician Wufeng and lower Silurian Longmaxi shales are widespread units in the Sichuan Basin, one of the most gas-productive sedimentary basins in China (Chen et al., 2011; Dai et al., 2014). Previous studies indicate that the Wufeng-Longmaxi shales in Sichuan Basin are characterized by a high organic matter (OM) content, large thickness, high thermal maturity, appropriate brittleness and strong gas-generation yield (Guo and Zhang, 2014; Guo et al., 2014a). For instance, shale gas production from the Wufeng-Longmaxi Formations in the Jiaoshiba area, the largest shale gas field in China, has exceeded  $300 \times 10^4 \text{ m}^3$  (105.9 Mmcf) (Guo et al., 2014a,b). Thus, the Wufeng-Longmaxi Formations are considered as the most promising gas shale units in China. Extensive sedimentologic studies have been presented in last 10 years, and a variety of lithofacies, including argillaceous shale, carbonaceous shale, siliceous shale, calcareous shale, and muddy siltstone, have been recognized in this interval (Jiang et al., 2013; Li et al., 2017 e.g.; Liang et al., 2014; Mou et al., 2014; Ran et al., 2016; Wang et al., 2016b; Zheng et al., 2013). In addition, pore characteristics of the Wufeng-Longmaxi Formations have also received close attention. Until now, most studies of pore characteristics of these shales were aimed at documenting variability in morphology and structure (e.g. Chen et al., 2013a; Guo et al., 2014b; Jiao et al., 2014; Shi et al., 2015; Tang et al., 2015; Tian et al., 2013; Wang et al., 2016a; Yang et al., 2016), and to show that OM pores are dominant in organic-rich units. Scant attention has been paid, however, to the variability of pore networks and pore abundance with regard to the inherent

heterogeneity of the shales. Investigating the relationship between shale facies and pores networks will add to the basic understanding of the factors that control distribution of porosity and reservoir for the Wufeng-Longmaxi Formations.

With samples from the Wufeng-Longmaxi Formations of northern Guizhou, the main purpose of this study is to (1) define the shale facies; (2) identify the pore types; (3) quantify pore abundance of each facies; (4) assess pore development and pore networks in each facies during burial diagenesis; and (5) evaluate the main factors that control shale porosity.

## 2. Geological setting

The South China Block, consisting mainly of the Yangtze and Cathaysia blocks, was attached to the margins of Gondwana during the Late Ordovician to Early Silurian (Fig. 1A) (Metcalfe, 1994, 2013). Although accretion of fragments with Cathaysian affinities to the Yangtze Block may have begun as early as Middle to Late Proterozoic time, the Ordovician-Silurian collision zone in the southeastern margin of the Yangtze Block probably reflects the final phase of accretion between the two blocks and leads the Yangtze Block to turn into a foreland basin (Metcalfe, 1994, 2013; Su et al., 2009). The Sichuan Basin is a part of the South China Block and is regarded as a silled epicontinental sea that was likely connected to the open ocean (Fig. 1A) (Chen et al., 2004; Chen et al., 1987; Rong and Chen, 1987). Ordovician-Silurian fine-grained strata, including the Wufeng, Guanyinqiao, and Longmaxi Formations, are distributed widely across the Sichuan Basin. Their deposition is considered the result of regressions and



transgressions that were initiated by migrations of foreland basin and forebulge (Su et al., 2009), as well as glacial advance and retreat (Melchin et al., 2013; Mitchell et al., 2011; Moreau, 2011; Schönlaub et al., 2011). According to recent research on paleotopography (Chen et al., 2017; Zhang et al., 2014, 2016), Tongye-1 well is located in proximal area (~5 km east of Tongzi County), whereas Xiye-1 well is located in distal area (~20 km south from Xishui County) (Fig. 1B). Both wells contain the Wufeng Formation, Guanyinqiao Formation, and Longmaxi Formations (Fig. 2). The Wufeng Formation, dominated by graptolite-bearing shales, is mainly of Katian and earliest Hirnantian age (Fig. 2) and resulted from a transgression that is linked to the Boda warming event (e.g. Armstrong et al., 2009; Brenchley and Storch, 1989; Fortey and Cocks, 2005). Characterized by beds of shelly fauna, the Guanyinqiao Formation is mainly of Hirnantian age (Fig. 2). The Longmaxi Formation is also mainly composed of graptolite-rich shales, and its deposition is linked to a transgression of earliest Rhuddanian age. It is much thicker than the prior two units (Fig. 2). In the northern Guizhou area, the thickness of the Wufeng-Longmaxi Formations can reach as much as 500 m thickness (Fig. 1C), but our target section is just about 30 m thick and only includes the Wufeng, Guanyinqiao and lower portions of the Longmaxi Formation (Fig. 2).

### 3. Materials and methods

Continuous drill cores from two wells were described at decimeter scale. Twenty seven samples were ion milled for high resolution SEM analysis (secondary electrons (SE), backscattered electrons (BSE), and cathodoluminescence (CL) imaging) at the Indiana University Shale Research Lab. A GATAN Ilion™ edge mill was used to polish samples. It is a cross-beam ion mill that produces a high quality polished area of up to 2 mm<sup>2</sup>. In addition, five larger samples (up to 10 mm diameter) from the set of twenty seven samples examined initially were ion milled with a modified GATAN 600 DuoMill™ for larger scale SEM imaging (Schieber et al., 2016). The milled sample surfaces were examined without conductive coating with a FEI Quanta 400 FEG in low vacuum

mode. The composition of particles within the examined area was tested by Energy disperse X-ray spectroscopy (EDS). Duplicates from the set of twenty seven samples examined initially were milled into powders for analysis of total organic carbon content (TOC) by a Costech elemental analyzer (EC4010) at the Indiana University Bloomington Stable Isotope Research Facility (SIRF). Sixty one samples for two wells were ground into powders for mineralogical composition analysis by X-ray diffraction, using a PANalytical XPert Pro Multipurpose Diffractometer at the Analytical Laboratory of the Beijing Research Institute of Uranium Geology.

Scanning electron microscopy (SEM) imaging is widely used to observe nm-scale pores and pore networks in shale samples (e.g. Desbois et al., 2009; Loucks et al., 2012; Milner et al., 2010; Schieber, 2013; Slatt and O'Brien, 2011). Point-counting pores within SEM images is a direct and established way to quantitatively assess shale porosity (e.g. Ko et al., 2017; Loucks et al., 2012; Milliken et al., 2013). The general pore abundance was examined via point counts in SEM images. Point counts (500 points to 1000 points) were made in 89 lower magnification pictures (average magnification = 5700×) from 26 samples to determine the percentages of minerals, mineral-hosted pores, amorphous organic matter, and structured kerogen. Porosity within amorphous organic matter was measured by point counts (1000 points to 1500 points) in higher magnification images (average magnification = 97000x). These higher magnification images of amorphous organic matter were randomly selected from the samples as mentioned above. The overall SEM-visible porosity,  $\Phi_{SEM}$ , is calculated by the equation below:

$$\Phi_{SEM} = (\Phi_{a-om} \times A\text{-OM \%}) + \Phi_{min}$$

where  $\Phi_{a-om}$  is the average porosity examined within amorphous organic matter via point counts in the higher magnification images; A-OM % is the enrichment of amorphous organic matter obtained from point counts in the lower magnification images; and  $\Phi_{min}$  is the mineral-hosted porosity calculated by point counts in the lower magnification images. For comparison with the SEM-visible porosity, helium

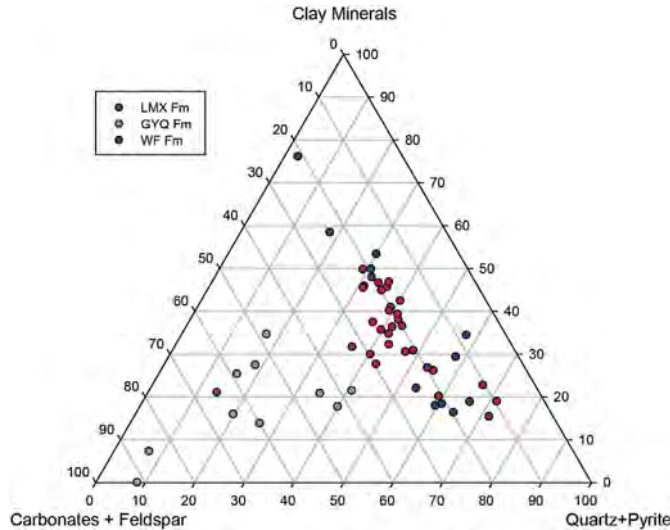


Fig. 3. Ternary diagram for the mineral composition (Loucks et al., 2012) of the Wufeng-Longmaxi Formations, northern Guizhou, South China.

porosities of four selected samples from the set of 26 sample were measured by the instrument of an ULTRAPORE-200A Helium porosimeter through the helium expansion method.

#### 4. Results and discussion

##### 4.1. Mineralogy

Samples from the Wufeng-Longmaxi succession contain quartz, clay minerals, calcite, dolomite, feldspar (k-feldspar and plagioclase) and pyrite (including marcasite). Quartz and clay minerals dominate in most samples from the Wufeng and Longmaxi Formations (29.1–75.4%, 12.7–58.4%, respectively), whereas carbonates, feldspar and pyrite are minor constituents (Fig. 3; Table 1). An exception is sample XY-13 from the Longmaxi Formation which is dominated by dolomite (62.5%) (Fig. 3; Table 1). In contrast to the Wufeng and Longmaxi Formations, the mineralogical composition of samples from the Guanyinqiao Formation is dominated by calcite and dolomite, with carbonate totals ranging from 32.67 to 91.6% (Fig. 3; Table 1). In contrast, quartz and clay minerals make only a small contribution to the overall composition (6.52–38.5%, 0–34.6%, respectively) (Fig. 3; Table 1). In vertical section, quartz contents decrease from the basal Wufeng to the uppermost Longmaxi section in both wells, whereas clay mineral abundance gradually increases upwards (Fig. 4).

##### 4.2. Lithofacies

Seven shale facies were identified in well Tongye-1 and well Xiye-1 (Li et al., 2017): (1) bioturbated claystones; (2) black siliceous shales; (3) black shales; (4) muddy fossiliferous shale; (5) black dolomitic siltstone; (6) gray muddy siltstone; and (7) dark gray muddy siltstones. Their stratigraphic distributions are shown in Fig. 2. Although shale and mudstone are both widely used terms for fine grained sediments, the term “shale” in the stratigraphic units (Wufeng and Longmaxi Shales) has been used for many years. In this research, we will therefore primarily use the term shale, with the understanding that it includes what some prefer to identify as mudstones.

##### 4.2.1. Bioturbated claystone

This facies was observed in the basal Wufeng Formation from both wells and contains about 50% clay minerals, 30% quartz, and 10% carbonates. The strata underlying this facies are gray muddy limestones of the Jiancaogou Formation. The majority of particles are smaller than

8  $\mu\text{m}$ . These bioturbated claystones are fully homogenized by bioturbation and lack any vestiges of distinct lamination (Fig. 5A and B) (Bioturbation index = 5; Taylor and Goldring, 1993; Lazar et al., 2015). Quartz grains are mostly detrital in origin (tested by CL; Schieber et al., 2000; Zinkernagel, 1978). Sulfides, including marcasite and pyrite, are scattered through the matrix. The bioturbated claystone shows higher TOC values in well Tongye-1 (up to 5.07%) than in well Xiye-1 (1.15–1.30%).

##### 4.2.2. Black siliceous shale

This shale facies is characterized by the highest quartz contents (50–70%) among all the lithofacies examined. The clay mineral content is relatively low, ranging from 12 to 27%. The dominant particle size is in the 8  $\mu\text{m}$ –32  $\mu\text{m}$  range. The facies is characterized by a succession of thin layers with indistinct boundaries which can also be described as “bands” (Fig. 5C). Some faint bands are marked by continuous or discontinuous silty laminae. Banding appears to reflect rapid deposition of fine-grained clastics with distinct compositional attributes, organic content, grain size variation, and horizontal cryptobioturbation (Wilson, 2012). Unlike laminae, bands are usually characterized by diffuse boundaries. Most quartz grains display dull red CL color, gray blue CL color or non-luminescent color (Fig. 6E and F, dwell time is 1000  $\mu\text{s}$  per pixel). According to classification of the CL color of quartz (Götze and Zimmerle, 2000), quartz grains with no CL or weakly luminescent color are authigenic origin. Thus, most quartz grains in this facies are authigenic. Carbonate grains are sparsely scattered through this facies, and some diagenetic calcite cement occurs within the matrix. Disseminated pyrite framboids are common within the matrix. This facies is enriched in organic matter, with TOC values ranging from 2.69% to 6.61%.

##### 4.2.3. Muddy fossiliferous shale

This facies contains an abundance of shelly fossils, and is characterized by interspersed fossil-rich layers. It typically forms stacked successions of fossil-rich layers that alternate with “background” rock that contains scattered fossil fragments. The composition of the background matrix changes from layer to layer, and proportions of minerals range from 6.5 to 57.6% for quartz, 16.8–84.6% for carbonate, and 7.2–27.4% for clay minerals. The background matrix of this facies is variable in well Tongye-1, with an upward progression from siltstone, to bioturbated micrite, and micrite (Fig. 5E, F, G). In well Xiye-1, in contrast, the background matrix is homogeneous and consists largely of siliceous shale (Fig. 5H). In general, the background matrix consists of diagenetic silica and calcite mixed with clay minerals. Disseminated grains of pyrite and euhedral marcasite are a common constituent. Diagenetic phosphate and phosphatic pellets are preserved within the matrix. In well Tongye-1 this facies is characterized by low TOC values (lower than 1%), whereas in well Xiye-1 it may contain as much as 3.5% TOC.

##### 4.2.4. Black shale

Similar to the black siliceous shale, this facies typically consists of stacked faint bands with parallel continuous or discontinuous silt laminae (Fig. 6A). However, it contains less quartz (33–45%) and has a higher proportion of clay minerals (30–40%) (Table 1). The average particle sizes range from 8  $\mu\text{m}$  to 32  $\mu\text{m}$ . Although authigenic silica is present in the shale matrix, detrital quartz grains dominate the quartz component (Fig. 6B). Pyrite framboids are widely disseminated through the matrix. The TOC content ranges from 2.88% to 9.10%.

##### 4.2.5. Black dolomitic siltstone

Interspersed with black shale intervals, this facies contains abundant dolomite (up to 62.5%) and was only observed in well Xiye-1 (Table 1). Black dolomitic siltstone typically consists of stacked successions of faint dolomitic bands and discontinuous silty laminae (Fig. 6C). Dolomite grains range in size from 30  $\mu\text{m}$  to 50  $\mu\text{m}$  (Fig. 6D).

**Table 1**

Mineralogical composition in the Wufeng-Longmaxi Formations, northern Guizhou, South China.

Code	Depth (m)	Lithofacies	Quartz (%)	K-feldspar (%)	Plagioclase (%)	Calcite (%)	Dolomite (%)	Pyrite (%)	Total clay (%)
<b>Well Tongye-1</b>									
KTY-29	643.80	Dark gray muddy siltstone	30.28	2.50	8.47	10.52	1.81	1.02	45.41
KTY-28	647.30		34.43	1.82	6.47	11.57	0.00	0.85	44.87
KTY-27	652.80	Gray muddy siltstone	40.70	3.30	10.10	10.10	0.00	1.10	34.70
KTY-26	654.90		35.27	4.89	16.16	10.05	1.30	0.71	31.62
KTY-25	656.35		39.80	2.70	11.40	10.50	0.00	0.00	35.60
KTY-24	659.80		38.92	1.90	5.47	10.83	1.22	2.37	39.29
KTY-23	661.30	Black shale	44.50	2.60	6.10	9.70	3.80	2.80	30.50
KTY-22	663.06		38.50	0.00	6.10	32.30	3.90	1.50	17.70
KTY-21	663.20		35.94	1.52	5.13	36.38	2.81	1.05	16.53
KTY-20	665.00	Muddy fossiliferous shale	18.52	1.11	4.07	59.06	0.00	1.30	15.94
KTY-19	665.20		8.40	0.00	0.00	91.60	0.00	0.00	0.00
KTY-18	665.45		6.53	0.00	0.88	84.64	0.00	0.67	7.27
KTY-17	666.60		13.90	0.00	0.00	47.70	11.10	2.00	25.30
KTY-16	667.25		17.60	0.97	4.22	44.84	4.02	0.95	27.40
KTY-15	667.30		14.50	0.00	1.60	34.70	11.90	2.70	34.60
KTY-14	669.15		23.40	2.56	7.51	45.88	4.02	2.84	13.80
KTY-13	670.00		29.54	2.11	9.54	27.78	4.88	5.37	20.77
KTY-12	670.50	Black siliceous shale	53.70	0.00	0.00	18.00	6.30	0.00	22.00
KTY-11	670.70		52.81	0.55	4.83	10.50	3.79	0.75	26.77
KTY-10	671.55		64.91	1.44	3.97	13.14	0.00	1.27	15.28
KTY-9	672.75		58.00	0.00	3.90	8.80	0.00	0.00	29.30
KTY-8	673.13		75.42	0.79	2.77	7.62	0.00	0.66	12.74
KTY-7	674.05		61.34	0.49	7.28	7.04	4.81	2.71	16.34
KTY-6	674.60		52.11	2.20	6.23	6.27	0.00	1.03	31.58
KTY-4	675.20		55.50	0.00	4.90	3.10	0.00	2.10	34.40
KTY-3	677.50	Bioturbated claystone	45.14	2.82	5.92	1.33	0.00	1.99	42.81
KTY-2	678.20		29.60	0.00	5.30	3.70	11.30	2.20	47.90
<b>Well Xiye-1</b>									
KXY-34	615.70	Dark gray muddy siltstone	29.10	0.00	6.50	7.00	7.70	0.00	49.70
KXY-33	618.00		29.80	0.00	7.00	7.50	8.40	1.50	45.80
KXY-32	618.40		35.70	4.20	10.20	3.60	2.00	3.40	40.90
KXY-31	621.30		34.50	3.00	9.90	5.50	0.00	1.50	45.60
KXY-30	624.75		34.60	0.00	8.80	8.60	0.00	1.20	46.80
KXY-29	626.70		37.90	3.00	7.80	6.00	3.90	1.30	40.10
KXY-28	627.00		38.70	1.40	8.60	3.80	3.50	1.60	42.40
KXY-27	628.50	Black shale	38.90	1.80	9.30	10.40	8.10	1.60	29.90
KXY-26	629.00		39.00	1.30	12.90	1.80	3.90	3.10	38.00
KXY-25	629.40	Black dolomitic siltstone	14.00	0.00	2.50	0.00	62.50	0.00	21.00
KXY-24	630.30	Black shale	29.80	0.00	6.50	13.10	0.00	4.00	46.60
KXY-23	630.80		40.20	2.40	9.40	5.80	4.40	1.50	36.30
KXY-22	631.00		40.00	0.80	13.70	1.20	4.20	3.60	36.50
KXY-21	632.50		33.20	1.60	4.50	12.70	6.50	4.10	37.40
KXY-20	633.00		39.80	2.20	16.90	1.10	4.50	3.30	32.20
KXY-19	635.00		45.00	1.80	5.80	9.70	3.20	3.70	30.80
KXY-18	636.00		55.70	1.60	3.60	7.90	7.60	3.50	20.10
KXY-17	636.50		45.00	1.80	5.80	9.70	3.20	3.70	30.80
KXY-16	636.90		39.50	0.00	2.70	8.20	18.70	3.30	27.60
KXY-15	637.30	Black siliceous shale	52.60	0.00	3.90	7.50	7.40	2.50	26.10
KXY-14	638.30		69.40	1.10	2.50	3.40	2.60	2.10	18.90
KXY-13	638.70		64.60	0.00	2.00	4.70	3.80	2.20	22.70
KXY-12	639.00		55.70	1.60	3.60	7.90	7.60	3.50	20.10
KXY-11	640.80		69.90	0.00	2.20	7.50	3.20	1.80	15.40
KXY-10	641.00		69.40	1.10	2.50	3.40	2.60	2.10	18.90
KXY-9	643.00		57.60	1.10	4.60	6.40	10.40	2.00	17.90
KXY-8	643.50		69.90	0.00	2.20	7.50	3.20	1.80	15.40

(continued on next page)

**Table 1** (continued)

Code	Depth (m)	Lithofacies	Quartz	K-feldspar	Plagioclase	Calcite	Dolomite	Pyrite	Total clay
			(%)	(%)	(%)	(%)	(%)	(%)	(%)
KXY-7	643.70	Muddy fossiliferous facies	37.70	0.00	3.10	21.80	12.70	3.30	21.40
KXY-6	644.20	Black siliceous shale	58.10	0.00	3.00	9.00	9.00	2.60	18.30
KXY-5	644.80		63.50	0.00	3.30	5.10	6.70	2.60	18.80
KXY-4	645.00		57.60	1.10	4.60	6.40	10.40	2.00	17.90
KXY-3	646.00		63.50	0.00	3.30	5.10	6.70	2.60	18.80
KXY-2	647.30	Bioturbated claystone	8.70	0.00	0.00	23.50	0.00	9.40	58.40
KXY-1	649.50		30.00	0.00	7.20	9.50	0.00	0.00	53.30

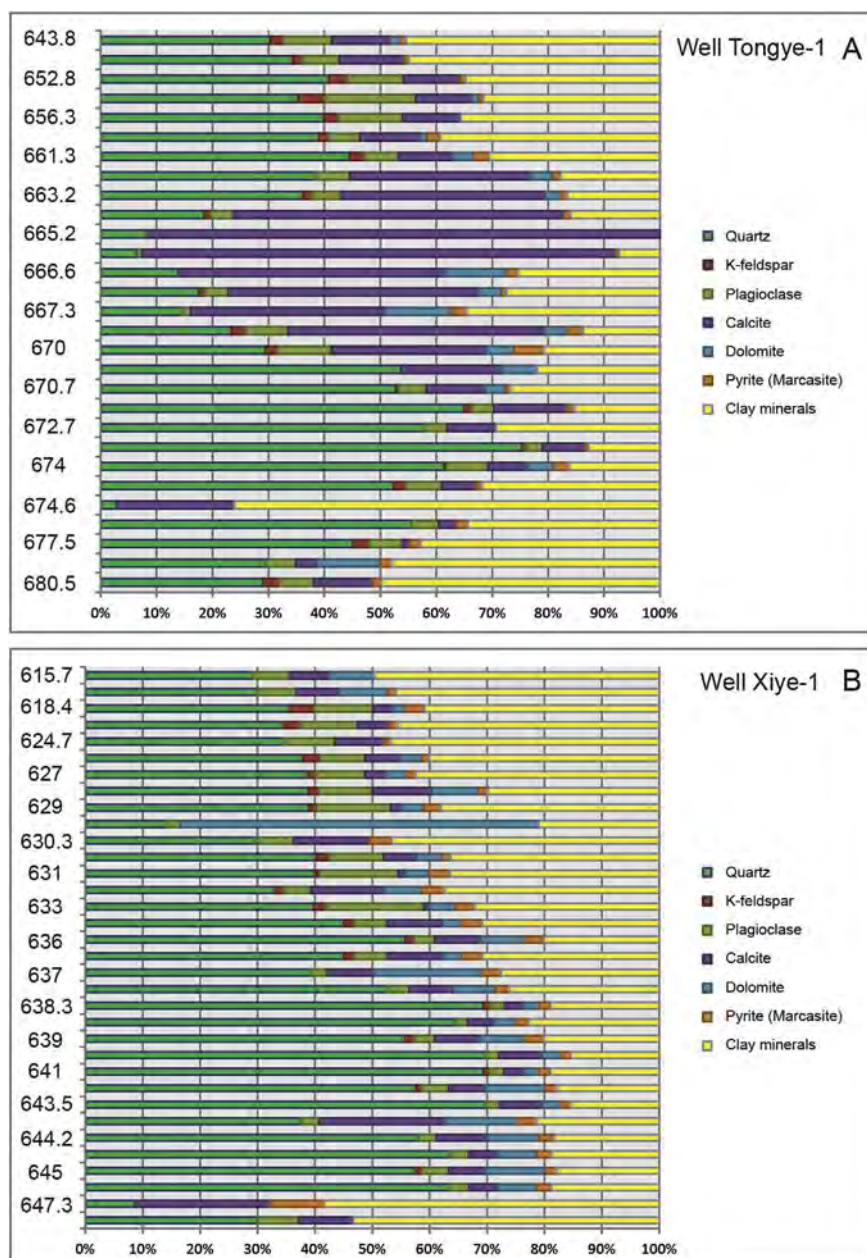


**Fig. 4.** Vertical variations of mineral composition in Well Tongye-1 and Well Xiyé-1. Vertical axis indicates sample depth within core.

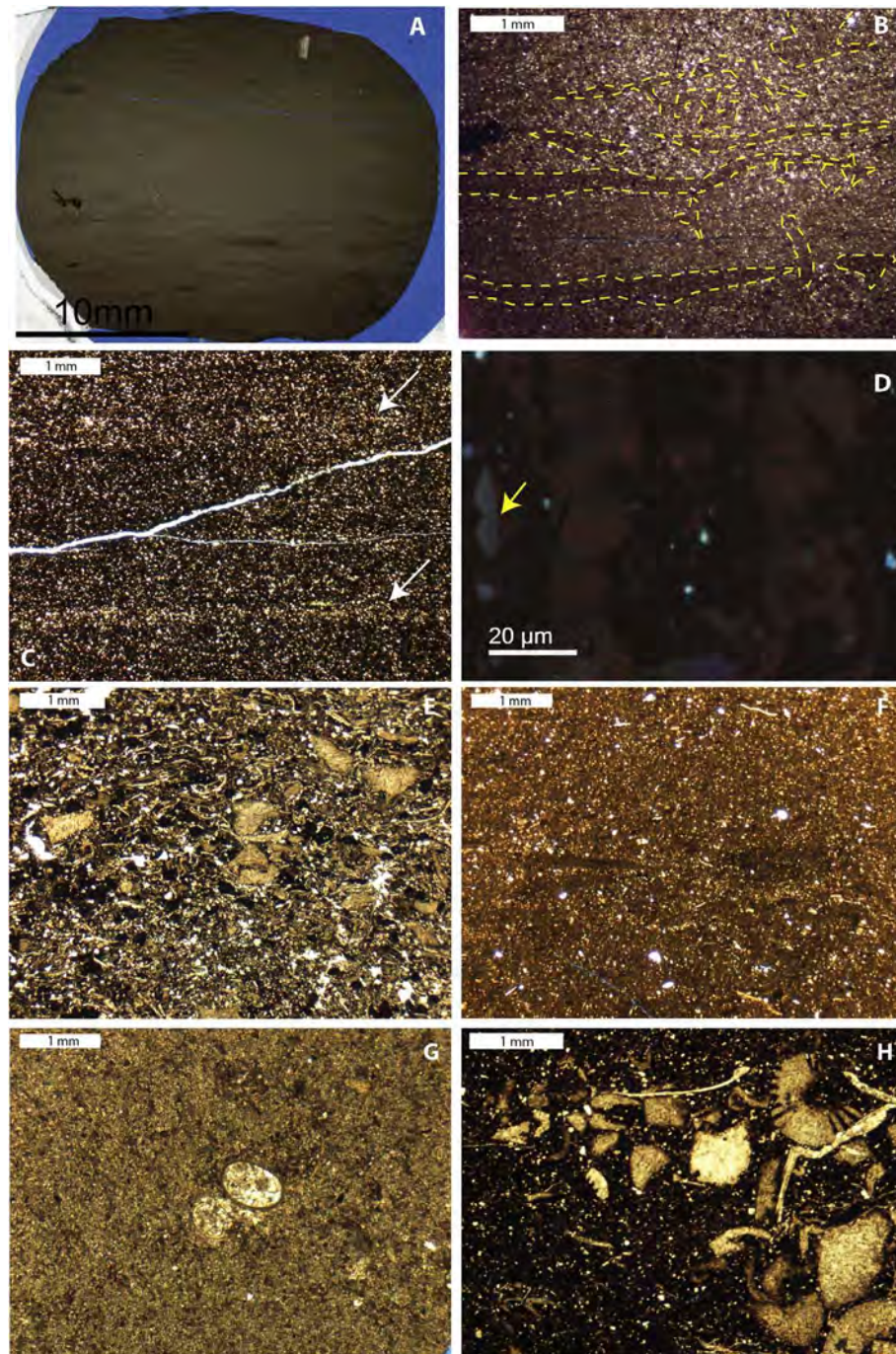


**Fig. 5.** Lithofacies in the Wufeng-Longmaxi Formations: Part I. (A) Photomicrograph of the bioturbated claystone (XY-2, 646.6 m). (B) Bioturbated features found in the XY-2 (outlined by dashed yellow line). (C) Photomicrograph of the black siliceous shale (XY-8, 638.7 m). Notice faint bands (indicated by white arrows). (D) CL image of the black siliceous shale (TY-8T, 676.1 m). Dull red CL and gray blue CL inside it indicate diagenetic silica and early diagenetic silica, respectively. Light blue CL in the left center (yellow arrow) indicates detrital silica (quartz). The imaged surface is perpendicular to bedding, and unlike in the other images of this facies, beds are oriented vertical. (E) Photomicrograph of a fossil-rich layer in a muddy fossiliferous facies (TY-3T, 669 m) of well Tongye-1. The background matrix is siltstone. (F) Photomicrograph of a muddy fossiliferous facies (TY-2T, 667.3 m) of well Tongye-1. The background matrix is dominated by bioturbated micrite. (G) Photomicrograph of a muddy fossiliferous facies (TY-1T, 666.6 m) of well Tongye-1. The background matrix is micrite. (H) Photomicrograph of a muddy fossiliferous facies (XY-5, 643.7 m) of well Xiye-1. The background matrix is siliceous shale. (For interpretation of the references to color in this figure legend, the reader is referred to the Web version of this article.)

The facies is characterized by a high TOC content (about 4.1%), and disseminated pyrite framboids are common in this facies as well.

#### 4.2.6. Gray muddy siltstone

This facies was only identified in well Tongye-1. The mineral content ranges from 35% to 40% for quartz, and 31%–35% for clay minerals (Table 1). Most of the quartz grains are silt size (35–60  $\mu\text{m}$ ) and of detrital origin. This facies is commonly organized into stacked successions of silty bands, bundles of silt laminae, and clay-rich layers (Fig. 6E). Contacts among these components are sharp, and no gradation of grain sizes within silty bands was observed (Fig. 6F). Coarser silts tend to accumulate in silt laminae and bands, whereas finer silt is dispersed among clays. Some silty laminae are well cemented by calcite.

#### 4.2.7. Dark gray muddy siltstone

Compared to gray muddy siltstone, dark gray muddy siltstone contains more clay minerals (40–46%) and less detrital quartz (30–39%) (Table 1). This facies was observed in both wells. It also forms stacked succession of silty bands, bundles of parallel silt laminae, and clay-rich layers (Fig. 6G and H). All these components show sharp bottom and top boundaries, and grains sorted into laminae without evidence of gradation. However, the proportion of silt within given bands can be quite variable.

#### 4.3. Pore types

During last several years, a variety of pore types in many shale successions have been identified (e.g. Curtis et al., 2010; Desbois et al., 2009; Loucks et al., 2012; Milner et al., 2010; Passey et al., 2010;

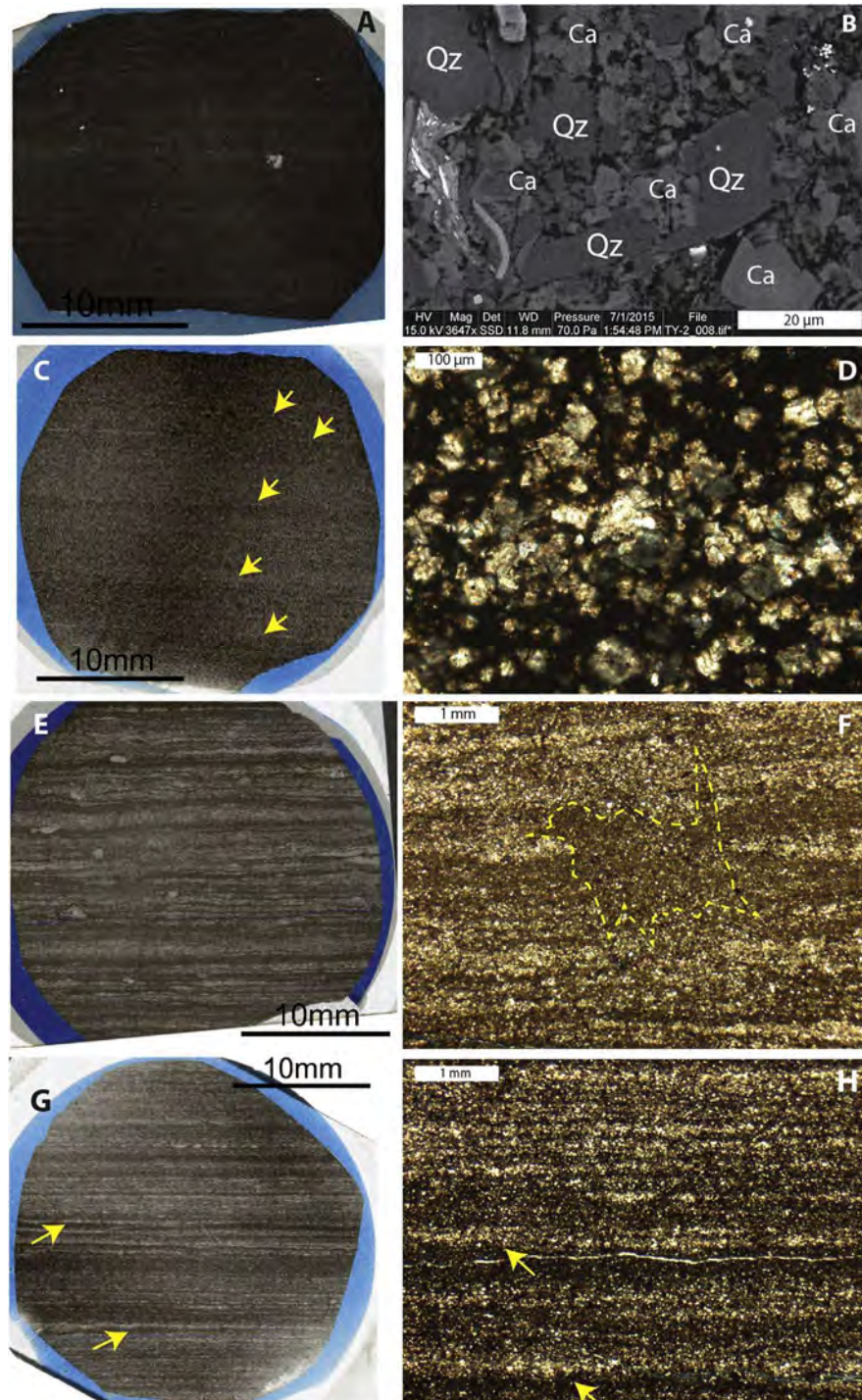


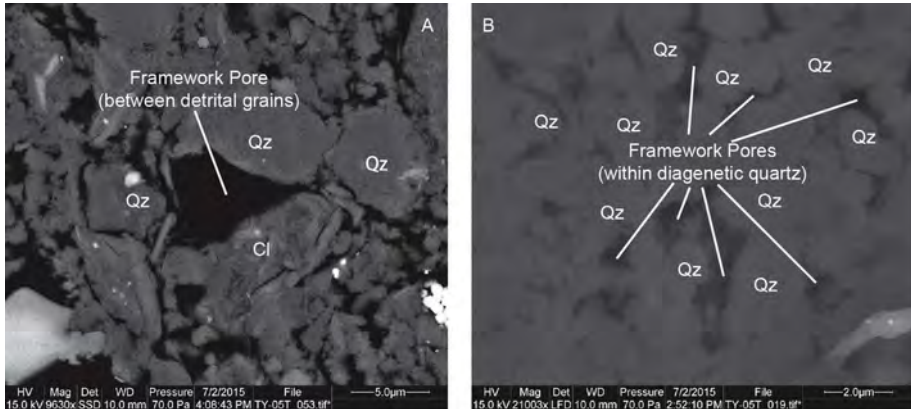
**Fig. 6.** Lithofacies in the Wufeng-Longmaxi Formations: Part II. (A) Photomicrograph of the black shale (XY-11, 629.2 m). Notice faint bands and parallel discontinuous laminae. (B) BSE image of the black shale (XY-11, 629.2 m). Notice disseminated detrital quartz and diagenetic calcite cement in the matrix. (C) Photomicrograph of the black dolomitic siltstone (XY-13, 629.4). Yellow arrows point to parallel discontinuous laminae. (D) Photomicrograph of dolomite (cross-polarized light) in sample XY-13. Note silt size of dolomite grains. (E) Photomicrograph of the gray muddy siltstone from well Tongye-1 (TY-7, 649.8 m). (F) Photomicrograph of silt bands interbedded with clay-rich layers. Note interruption of silty layers by bioturbation (outlined by yellow dashed line). (G) Photomicrograph of the dark gray muddy siltstone (XY-14, 624.7 m). Silty bands are interbedded with clay-rich layers. Yellow arrows point to scouring surfaces. (H) Close-up of silty bands interbedded with clay-rich layers (XY-14, 624.7 m). Yellow arrows point to scouring surfaces. Plane-polarized light image. (For interpretation of the references to color in this figure legend, the reader is referred to the Web version of this article.)

Schieber, 2010, 2013; Slatt and O'Brien, 2011). According to petrographic observation by Schieber (2010, 2013), a finite number of pore types exist in spite of considerable variability in composition, depositional setting, and compaction history. Thus, the nomenclature outlined by Schieber (2010, 2013) is mainly followed. On the basis of visual examination of numerous SEM pictures of all the facies, four main pore types were observed: (1) framework pores, (2) intrapores, (3) phyllosilicate framework (PF) pores, and (4) OM pores. The following section summarizes characteristics of each pore type, respectively.

#### 4.3.1. Framework pores

Framework pores are defined as void spaces preserved among rigid

grains, such as detrital grains (i.e., quartz, feldspar and shale clasts), carbonate grains, and/or authigenic rigid minerals (quartz, pyrite and marcasite) (Fig. 7). This pore type is mostly comparable to the term “interparticle pore” as defined by Loucks et al. (2012). Framework pores between primary detrital grains are found in all facies except the black dolomitic siltstone (Fig. 7A). Most of them are variably collapsed and reduced in abundance in response to compaction during deep burial. Framework pores typically are randomly scattered and poorly connected. Pores show a wide size distribution, ranging from about 20 nm to 20 μm. Framework pores between authigenic minerals, especially authigenic silica, show different morphology and size distribution when compared to detrital-grain framework pores. Pores defined by authigenic silica are



characterized by variable shapes and are well preserved and connected (Fig. 7B). They show relatively narrow size distribution and range in width from about 10 nm to 3 µm. Most of the authigenic silica is likely derived from dissolution of biogenic opal (i.e., radiolarians) and was reprecipitated early in diagenesis in pore spaces of uncompact sediment (Schieber et al., 2000). In addition, some authigenic quartz may also have formed later in diagenesis during the smectite-to-illite transformation (Day-Stirrat et al., 2010; Hayes, 1991; Land and Milliken, 2009; Schieber, 2010; Surdam et al., 1991), occluding primary pore space and forming secondary framework pores. Both detrital-grain and authigenic-grain framework pores are locally occluded with organic matter or with authigenic clay platelets (Fig. 7).

#### 4.3.2. Intrapores

Intrapores, mainly consisting of dissolution features and intercrystalline pores, were observed in all lithofacies. Dissolution pores are

mostly developed in chemically unstable minerals (i.e., calcite, dolomite, and feldspar) (Fig. 8A and B) or fossils. Most of these pores show variable shapes and have lengths from 50 nm to 15 µm. This pore type is poorly developed overall, even in the carbonate-rich facies. Many tiny isolated "intrapores" (100-nm range) were observed within carbonate minerals and/or quartz grains (Fig. 8C and D), and these are interpreted as fluid inclusions that were cut open during the ion milling process. They are isolated and do not contribute to permeability.

Intercrystalline pores are void spaces preserved between crystals within diagenetic grains such as pyrite framboids, marcasite and phosphatic pellets (Fig. 9). In the Wufeng-Longmaxi Formations, intercrystalline pores are commonly preserved in pyrite framboids (Fig. 9A and B). Formation of pyrite framboids is closely associated with sulfate reduction within organic-rich sediments (Taylor and Macquaker, 2000), and thus there is a close association between framboidal pyrite and organic-rich facies. Most intercrystalline pores are tiny



**Fig. 8.** Characteristics of dissolution pores and Fluid inclusions. (A) Dissolution pores within calcite (BSE image), Longmaxi Formation, Well Xiye-1; (B) Dissolution pores within feldspar (BSE image), Wufeng Formation, Well Tongye-1; (C) Fluid inclusions within quartz (SE image), Longmaixi Formation, Well Xiye-1; (D) Fluid inclusions within dolomite, Guanyinqiao Formation, Well Tongye-1. Ca = calcite; Do = dolomite; Qz = quartz; Fe = feldspar. All the surfaces in SEM images are perpendicular to bedding. In these images bedding is oriented vertical.

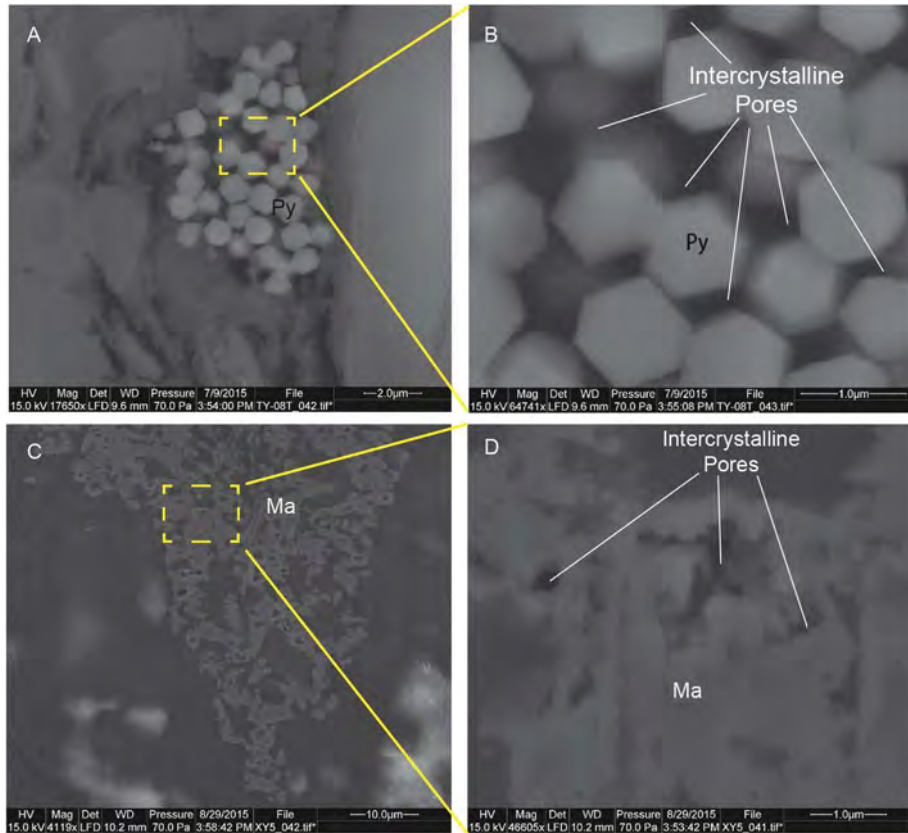


**Fig. 9.** Characteristics of intercrystalline pores. (A) Intercrystalline pores within pyrite framboids (SE image); (B) Close-up image of Intercrystalline pores within pyrite framboids (SE image); (C) Intercrystalline pores among marcasite crystals (SE image); (D) Close-up image of intercrystalline pores among marcasite crystals (SE image). Py = pyrite; Ma = marcasite. All the surfaces in SEM images are oriented perpendicular to bedding. In these images bedding is oriented vertical.

(60 nm–640 nm) but well-connected in three dimensions. Pyrite framboids are scattered through the shale matrix, and thus intercrystalline pores within them contribute a small portion of porosity. Intercrystalline pores were also observed in the secondary marcasite grains, ranging in size from 20 nm to 1  $\mu\text{m}$  (Fig. 9C and D).

#### 4.3.3. Phyllosilicate framework pores

Phyllosilicate framework (PF) pores are a ubiquitous pore type in all the facies. These void spaces are defined by a lattice-work of randomly oriented clay mineral platelets (Schieber, 2013). PF pores are comparable to the pores between or within clay aggregates in the spectrum of pore types outlined by Loucks et al. (2012). In the Wufeng-Longmaxi succession, two kinds of phyllosilicate framework pores could be recognized: primary PF pores and secondary PF pores (Fig. 10). Primary PF pores are pores preserved between detrital clay minerals, and most of them are best developed in pressure shadows adjacent to rigid compaction resistant grains and in spaces between such grains (Fig. 10A and B). Pores are well connected in three dimensions and are mostly triangular and sheetlike, ranging in size from 13 nm to more than ten  $\mu\text{m}$ . Secondary PF pores are defined as void spaces preserved between secondary clay minerals. Most of the latter are developed in association with secondary illite (Fig. 10C and D) that was produced later in diagenesis during the smectite-to-illite transformation (Day-Stirrat et al., 2010; Hayes, 1991; Land and Milliken, 2009; Schieber, 2010; Surdam et al., 1991). Diagenetic clay minerals fill in primary framework pores and form new secondary PF pores. Some of these clay minerals are clamped and propped by diagenetic cements. Sizes of these pores are very small, ranging in length from 16 nm to 85 nm. Connectivity of these pores is well developed. In addition, iron released from biotite or chlorite during late diagenesis, resulted in precipitation of euhedral pyrite (Schieber, 2011). The latter will prop up spaces between biotite or chlorite flakes, inducing development of secondary PF pores (Fig. 10E and F). These sheet-like pores have length range from 16 nm to 860 nm and are poorly connected.

#### 4.3.4. Organic matter pores

Organic matter (OM) pores are defined as pores that are found within organic matter (Loucks et al., 2012). Two types of organic matter were observed in the Wufeng-Longmaxi succession: structured organic matter and amorphous organic matter. Structured organic matter retains the morphologic features of graptolites that is abundant in the Wufeng-Longmaxi Formations and is the most readily identified variety of structured organic matter throughout the late Ordovician to the early Silurian. Amorphous organic matter mostly presents as irregular patches that fill spaces between mineral grains and probably represents bitumen (Schieber, 2013). Structured organic matter lacks of organic matter pores, although organic petrography (Shi et al., 2015) suggests the rocks to be gas mature (Fig. 11A and B). Amorphous organic matter by contrast, presumed to be bitumen at this maturity level, contains abundant organic matter pores. Two main types of OM pores were observed: foam type and bubble type (Schieber, 2013, Fig. 11C; D, E, F). Foam pores are rather abundant within organic matter but are relatively tiny, ranging in size from 3 nm to 145 nm (Fig. 11C and D). Bubble pores, in contrast, are not as abundant but substantially larger. Most of them are around 300 nm, with a size range from 85 nm to 1.3  $\mu\text{m}$  (Fig. 11E and F). The rounded bubble pores in particular suggest formation in fluid phase, possibly bitumen (Bernard et al., 2012). The close spatial association with foam pores suggests a common origin for both types of OM pores (Schieber, 2013). According to point counts, the average porosity in amorphous organic matter is 30.50%, with a range from 18.10% to 40.69% (Table 2). Typically, authigenic minerals such as quartz and illite are mixed with amorphous organic matter (Fig. 11E and F), which suggests that hydrocarbon generation and migration occurs after, or overlapping with smectite-to-illite transformation and the newly produced bitumen filled secondary voids between authigenic minerals (Schieber, 2013).

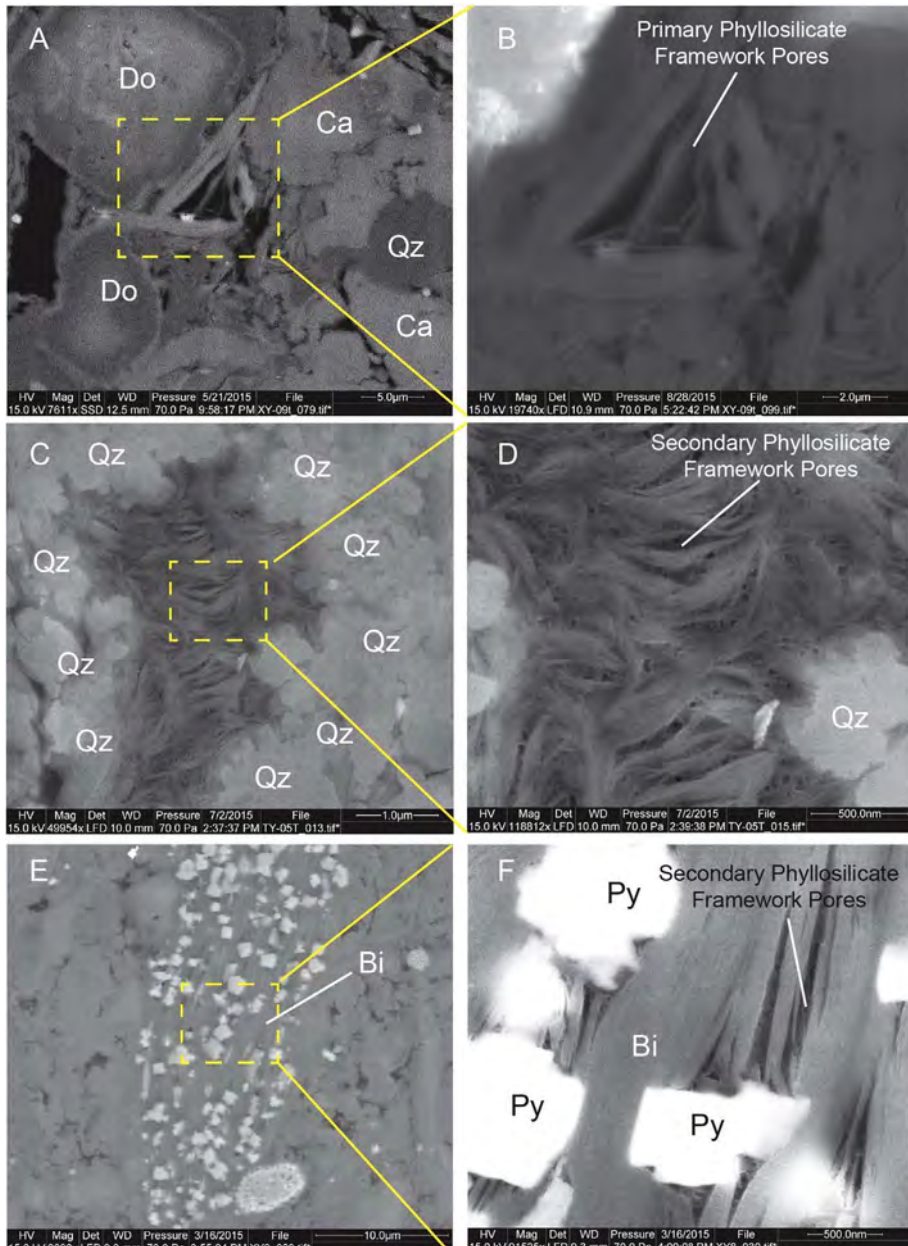


**Fig. 10.** Characteristics of phyllosilicate framework (PF) pores. (A) and (B): Primary phyllosilicate framework pores within chlorite which is surrounded by rigid grains, Wufeng Formation, Well Tongye-1; (C) and (D): Secondary phyllosilicate framework pores within diagenetic illite. These secondary illite minerals are surrounded by authigenic quartz (SE images). (E) and (F): Secondary phyllosilicate framework pores within biotite (SE images), Longmaxi Formation, Well Xiye-1. Ca = calcite; Do = dolomite; Qz = quartz; Py = pyrite; Bi = biotite. All the surfaces in SEM images are perpendicular to bedding. In these images bedding is oriented vertical.

#### 4.4. Pore networks and associated pore abundance and distribution

Any given shale facies may be dominated by one type of pore or a combination of several pore types. Pore networks and pore distribution in a given shale facies are highly controlled by mineralogy and sedimentary features. As described before, seven lithofacies were recognized in the Wufeng-Longmaxi succession, and show varieties of mineralogical compositions and sedimentary fabrics. Therefore, pore networks and distribution should be variable from facies to facies. In the following section, pore networks are described in the context of the various lithofacies identified in this study.

##### 4.4.1. Bioturbated claystones

Bioturbated claystones have the highest clay-mineral contents (47.95–50%), and moderate quartz enrichment (about 30%) (Table 1). Most of quartz grains are of detrital origin. Contents of chemically unstable minerals are relatively low, with 10–23% carbonate and 5–7% feldspar. Thus, the dominant inorganic pores are primary PF pores and framework pores (Fig. 12 A, B, C). Secondary PF pores and framework

pores between authigenic quartz were observed in some places. A few isolated fluid inclusions were found in scattered carbonate grains (Fig. 12D). Intercrystalline pores occur within sparsely disseminated framboidal pyrite and marcasite grains. At TOC values of 1.15–1.3%, organic matter is sparsely distributed within the background matrix. Framework pores mentioned above are largely occluded by amorphous organic matter (bitumen). Within this pore-filling OM, OM pores, especially foam pores, are well developed within organic matter (Fig. 12C, E). The average point-counting derived porosity of this facies is about 1.80% (Table 3).

##### 4.4.2. Black siliceous shales

Black siliceous shales contain very high quartz contents (50–75%) (Table 1), and most of that quartz is of authigenic origin. Framework pores defined by authigenic quartz grains, most of them comparatively small, are the dominant pores of this facies (Fig. 13 A, B). Clay mineral content is comparatively small, ranging from 12 to 27%, which results in poor preservation of PF pores. Some dissolution pores occur associated with carbonate grains, but contribution to total porosity is small

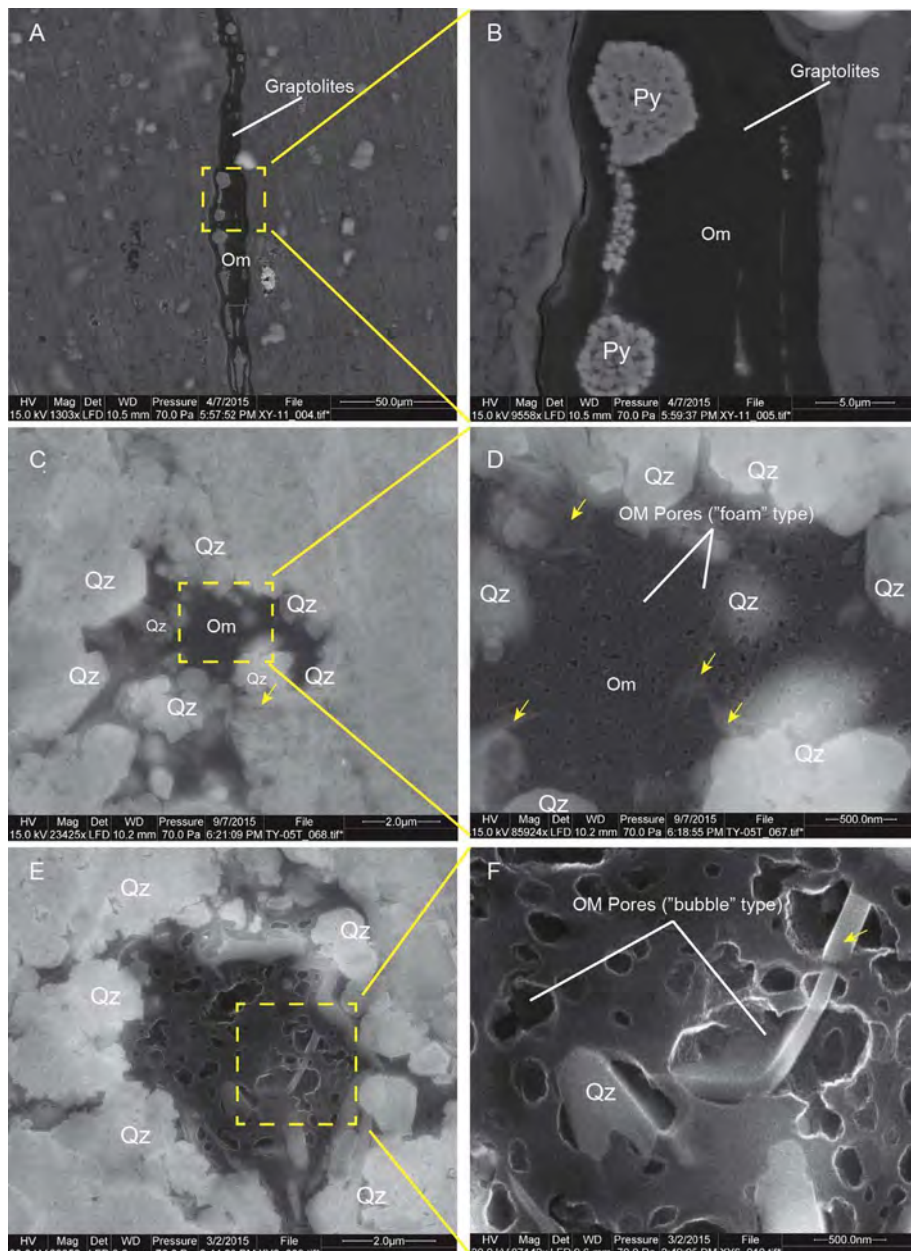


**Fig. 11.** Characteristics of organic matter (OM) pores. (A) and (B): Structured organic matter from graptolites (SE images). No pores are found within structured organic matter. (C) and (D): Foam pores in amorphous organic matter. Pore sizes range from 3 nm to 145 nm. Yellow arrows point to clay minerals (illite), Longmaxi Formation, Well Xiye-1. (E) and (F): Bubble pores in amorphous organic matter. Pore sizes range from 85 nm to 1.3 μm. Yellow arrows point to clay minerals, Longmaxi Formation, Well Xiye-1. Qz = quartz, Om = organic matter, Py = pyrite. All the surfaces in SEM images are perpendicular to bedding. In these images bedding is oriented vertical. (For interpretation of the references to color in this figure legend, the reader is referred to the Web version of this article.)

**Table 2**  
OM porosity within amorphous organic matter.

Sample	Pore type	Image	OM <sup>a</sup> (%)	$\Phi_{\text{a-om}}$ (%)
TY-05T	foam type	TY-05T-018	73.36	26.64
XY-6	bubble type	XY-6-010	59.31	40.69
XY-8	bubble type	XY-8-023	63.20	36.80
	bubble type	XY-8-045	75.75	24.25
	bubble type	XY-8-046	67.00	33.00
XY-10	foam type	XY-10-025	78.36	21.64
XY-4	foam type	XY-4-034	81.90	18.10
Average			69.50	30.50

<sup>a</sup> OM (%) = percentage of non-porous amorphous organic matter;  $\Phi_{\text{a-om}}$  (%) = percentage of scanning electron microscopy-visible porosity within amorphous organic matter.

because carbonate contents are commonly lower than 20%. Pyrite frambooids are disseminated through the shale matrix, within intercrystalline pores preserved within them. The facies is enriched in organic matter (average TOC value is 4.35%), which leads to wide

distribution of organic matter through the background matrix. Almost all mineral-hosted pores are filled with amorphous organic matter, in which well-connected OM pores are pervasively developed (Fig. 13 C, D, E). The porosity of this facies ranges in percentage from 2.88% to 6.54%, with an average porosity of 4.96% (Table 3).

#### 4.4.3. Black shales

Black shales contain less quartz (33–45%) and more clay-minerals (30–40%) than black siliceous shales (Table 1). Because detrital quartz grains dominate the quartz components, framework pores within authigenic quartz grains are fewer when compared to the black siliceous shales (Fig. 14A and B). Relict framework pores between detrital rigid grains could be observed (Fig. 14B). Because of a mixture of rigid and ductile grains, some primary PF pores are preserved in pressure shadows adjacent to larger compaction-resistant, rigid grains (Fig. 14C). A few primary PF pores occur within the matrix. A small population of isolated fluid inclusions within carbonate grains (Fig. 14D) as well as intercrystalline pores within pyrite frambooids were observed. This facies is also characterized by high TOC values (average content is

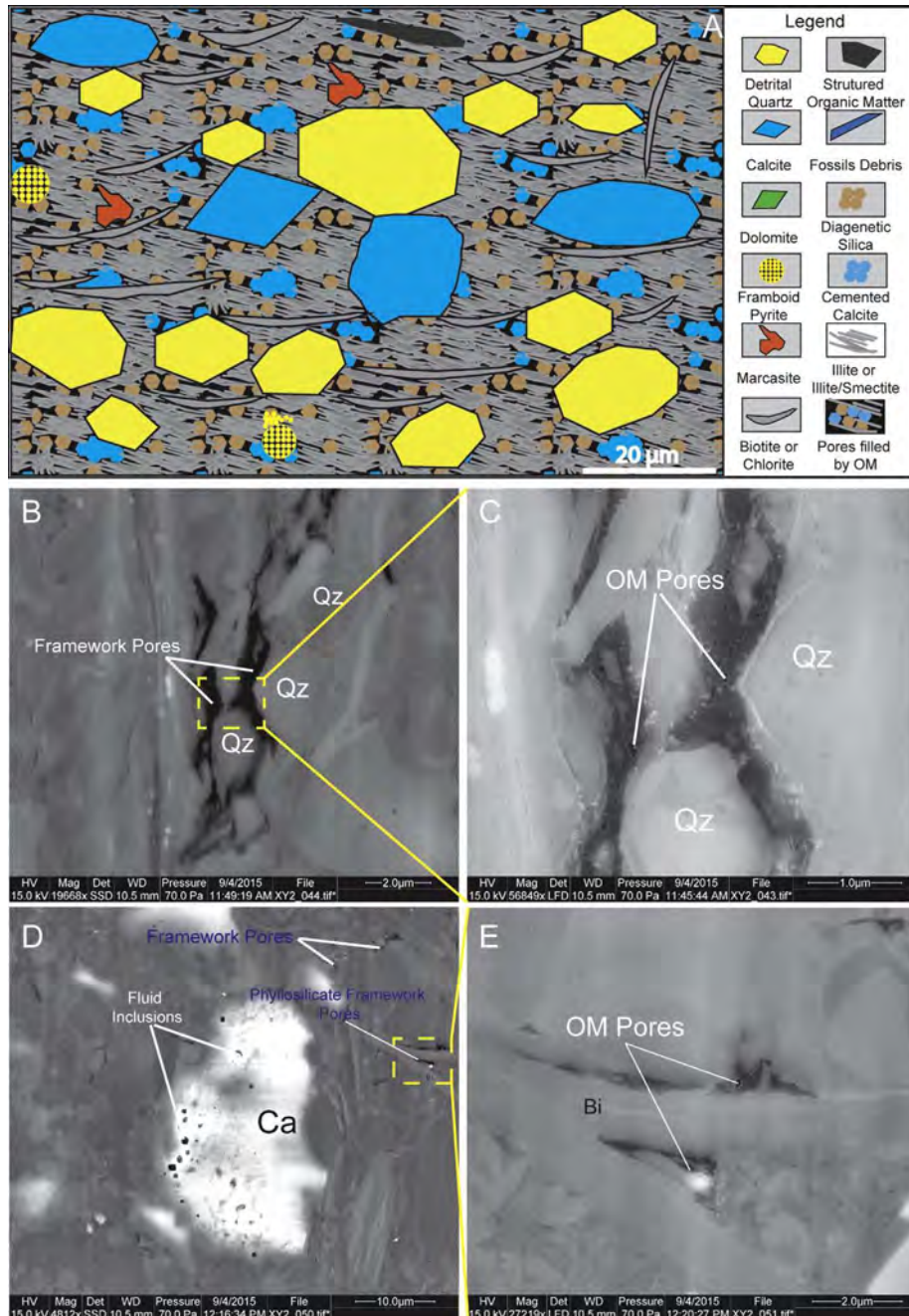


**Fig. 12.** Pore network of bioturbated claystones. (A) Generalized schematic diagram of pore network in bioturbated claystones. (B) Primary framework pores in the bioturbated claystone (BSE image), Wufeng Formation, Well Xiye-1. (C) Primary framework pores are filled with amorphous organic matter (Close-up SE image). OM pores are well developed within organic matter. (D) Fluid inclusions, framework pores and primary PF pores in the bioturbated claystone (BSE image), Wufeng Formation, Well Xiye-1. (E) PF pores are occluded by amorphous organic matter. OM pores are developed in organic matter. Qz = quartz; Ca = calcite; Bi = biotite. All the surfaces in SEM images are perpendicular to beddings. In images B-E bedding is oriented vertical.

5.07%). Similar to the black siliceous shales, amorphous organic matter fills mostly interstitial spaces between mineral grains, and OM pores are well developed within it (Fig. 14C, E). The SEM detectable porosity ranges from 2.24% to 4.43%, with an average value of 3.41% (Table 3).

#### 4.4.4. Muddy fossiliferous shale

Samples of muddy fossiliferous shale are commonly characterized by very high carbonate contents (32.6%–91.6%), and have relatively low quartz (6.5–35.9%) and clay mineral contents (7.2–27.4%) (Table 1). Framework pores between carbonate grains and/or fossils fragments are the main inorganic pore type of this facies (Fig. 15B). Many isolated fluid inclusions within carbonate grains and fossil fragments were observed (Fig. 15C). As described in the *Lithofacies* section, the background matrix of this facies shows obvious heterogeneity from proximal (well Tongye-1) to distal (well Xiye-1), leading to significant changes with regard to the contents of authigenic quartz and clay

minerals. Therefore, preservation of pores related to authigenic quartz grains and clay minerals varies accordingly. Generally speaking, the background matrix of muddy fossiliferous shale in well Xiye-1 is dominated by black siliceous shale, so framework pores between authigenic quartz grains as well as PF pores are relatively well preserved (Fig. 15D). In contrast, the background matrix of this facies in well Tongye-1 is mainly micrite, so few pores related to authigenic quartz and clay minerals are developed (Fig. 15E). A few intercrystalline pores within frambooidal pyrite and marcasite grains occur within the matrix. The facies in well Xiye-1 this facies is enriched in organic matter (about 3.5%), whereas TOC values of this facies in well Tongye-1 are typically below 1%. Therefore, inorganic pores of this facies in well Xiye-1 are mostly filled by porous amorphous organic matter (foam and bubble pores in OM), whereas the inorganic pores of this facies in well Tongye-1 typically have stayed open. The average porosity of this facies in well Tongye-1 is about 1.82%, and in well Xiye-1 it is about 2.14% (Table 3).

**Table 3**  
Total SEM-visible porosity in Wufeng-Longmaxi Formations, northern Guizhou, South China.

Lithofacies	Sample	Number of images	MIN <sup>a</sup> (%)	A- OM <sup>a</sup> (%)	$\Phi_{\min}^{\text{a}}$ (%)	S-OM <sup>a</sup> (%)	$\Phi_{\text{SEM}}^{\text{a}}$ (%)	TOC(%)	$\Phi_{\text{He}}^{\text{a}}$
Faintly Banded Black Siliceous Shales	TY-08T	4	79.79	19.66	0.55	0.00	6.54	6.61	\\\\\\\\
	TY-07T	5	81.44	16.60	0.71	1.25	5.77	4.89	\\\\\\\\
	TY-06T	3	83.69	15.58	0.51	0.22	5.26	5.46	\\\\\\\\
	TY-05T	3	87.91	11.59	0.51	0.00	4.04	4.38	\\\\\\\\
	TY-04T	3	79.07	20.80	0.14	0.00	6.48	4.17	\\\\\\\\
	XY-4	5	79.99	16.43	0.30	3.28	5.31	5.77	4.40
	XY-8	2	89.22	10.58	0.20	0.00	3.43	3.29	\\\\\\\\
	XY-9	2	88.80	9.43	0.00	1.77	2.88	3.67	2.10
	XY-2	2	96.93	1.83	1.24	0.00	1.80	1.15	\\\\\\\\
Bioturbated Claystones	TY-09	5	86.53	11.16	0.78	1.52	4.18	5.07	\\\\\\\\
	XY-13	4	94.57	5.00	0.43	0.00	1.95	4.10	\\\\\\\\
Faintly Banded Black Dolomitic Siltstone	TY-02T	5	98.15	0.00	1.85	0.00	1.85	0.66	2.12
Muddy Fossiliferous Shale	TY-1	3	98.20	0.00	1.80	0.00	1.80	0.93	1.86
Faintly Banded Black Shales	XY-5	5	95.13	3.93	0.94	0.00	2.14	3.51	\\\\\\\\
	TY-2	5	86.07	13.67	0.27	0.00	4.43	9.10	\\\\\\\\
	TY-4	6	89.53	6.37	0.30	3.80	2.24	5.27	\\\\\\\\
	XY-11	5	85.60	10.65	0.21	3.53	3.46	2.88	\\\\\\\\
Banded Gray Muddy Siltstone: Clay-rich layer	XY-12	5	88.99	10.77	0.24	0.00	3.52	3.02	\\\\\\\\
	TY-8	4	98.73	0.77	0.50	0.00	0.74	\\\\\\\\	\\\\\\\\
Banded Gray Muddy Siltstone: Silty laminae	XY-17	1	98.60	1.20	0.20	0.00	0.57	1.10	\\\\\\\\
Banded Gray Muddy Siltstone: Silty bands	XY-18	1	95.40	4.20	0.40	0.00	1.68	1.24	\\\\\\\\
	TY-5	2	98.30	0.00	1.70	0.00	1.70	0.50	\\\\\\\\
	XY-14	3	93.23	6.03	0.68	0.00	2.52	0.96	\\\\\\\\
	XY-15	3	97.88	1.69	0.43	0.00	0.95	1.23	\\\\\\\\
	XY-17	1	97.80	1.50	0.70	0.00	1.16	1.10	\\\\\\\\
	XY-19	1	95.11	4.67	0.22	0.00	1.64	1.32	\\\\\\\\

<sup>a</sup> MIN (%) = percentage of minerals; A-OM (%) = percentage of amorphous organic matter;  $\Phi_{\min}$  (%) = percentage of mineral-hosted porosity. S-OM (%) = percentage of structured organic matter;  $\Phi_{\text{SEM}}$  (%) = percentage of total scanning electron microscopy -visible porosity.  $\Phi_{\text{He}}$  (%) = percentage of helium porosity.

#### 4.4.5. Black dolomitic siltstone

The facies contains abundant dolomite (up to 62.5%) and relatively low quantities of quartz and clay minerals, about 14% and 12%, respectively (Table 1). Framework pores between dolomite grains and fluid inclusions within dolomite are common throughout this facies (Fig. 16A and B). The background matrix is dominated by authigenic quartz and clay minerals, and framework pores between authigenic quartz grains as well as PF pores are preserved (Fig. 16B and C). Pyrite framboids are widespread through the matrix and contain inter-crystalline pores (Fig. 16D). The TOC content of this facies is comparatively high (up to 4.10%), and therefore the pores mentioned above are occluded by amorphous organic matter (Fig. 16E). Within this organic matter OM pores are well developed. The SEM visible porosity is about 1.95% (Table 3).

#### 4.4.6. Muddy siltstones

Both gray and dark gray muddy siltstones have similar abundances of quartz and clay minerals, ranging from 30% to 45% (Table 1). In addition, these two facies are also rather similar with regard to sedimentary structures as described in the *Lithofacies* section. Therefore, pore networks and distributions are quite similar. Unlike the other facies described so far, these two facies show obvious heterogeneity and are characterized by alternation of silty laminae, silty bands and clay-rich layers (Fig. 17A and B). So pore network styles change from layer to layer. Silty laminae are dominated by silt-size detrital grains mixed with very small amounts of clay minerals and organic matter (Fig. 17C). Due to burial compaction silt grains, if elongate, tend to be aligned horizontally. The few framework pores that remained after burial compaction are fully cemented by diagenetic calcite (Fig. 17C). Therefore, pores are not well developed within silty laminae. In silty bands, detrital grains are overall smaller and there is appreciable admixture of clay minerals. Admixture of rigid silt grains and ductile clay flakes resulted in preservation of some primary PF pores within silty bands (Fig. 17D). Clay-rich layers are dominated by high clay-mineral contents and a paucity of detrital rigid grains. The latter are generally

small and scattered and do not provide effective pressure shadows for preservation of primary PF pores. The clay mineral fabric is therefore tightly compacted with few PF pores (Fig. 17E). Shrinkage cracks occurs commonly within clay-rich layers (Fig. 17E) and are interpreted as artifacts of sample dehydration (Loucks et al., 2012). Therefore, clay-rich layers generally do not contribute to porosity and permeability in these facies. Pyrite framboids with interstalline pores are scattered throughout the muddy siltstones. TOC values are relatively low (average TOC value is 1.08%), so only a portion part of the mineral-hosted pores are filled with amorphous organic matter that contains foam-type organic matter pores. The porosities of silty laminae and clay-rich layers are relatively low (are 1.32% and 0.74% average porosity respectively). In contrast, silty bands are more porous, ranging from 0.95% to 2.52% (Table 3).

It is worthwhile to note that porosity calculated by point-counting method has some disadvantages: (1) the SEM visible porosity may have limited relevance if ion-milling conditions caused surface artifacts; (2) only cover very small areas which may or may not be representative of the rock overall; (3) very small pores (< 2 nm) cannot be detected by SEM. In present research, the procedure proposed by Schieber et al. (2016) was followed to minimize/eliminate misinterpretation of surface artifacts. To verify accuracy of the SEM visible porosity, helium porosities of four selected samples were measured. The data of helium porosity is well correlated with the corresponding data of the SEM visible porosity (Table 3). In addition, porosity of this organic-rich interval around the study area was measured by He-Hg method or other methods in recent publications (Chen et al., 2013b; Guo et al., 2016; Li et al., 2016; Qin et al., 2017; Wang et al., 2013, 2014, 2017). These data suggest that porosity of the Wufeng-Longmaxi interval has a range of 2%–10%. Thus, the SEM visible porosity of this study (up to 6.54%) is consistent with previous studies and has relative significance.

#### 4.5. Effect of organic matter on porosity

OM pores, usually as nanopores, play a significant role in the pore

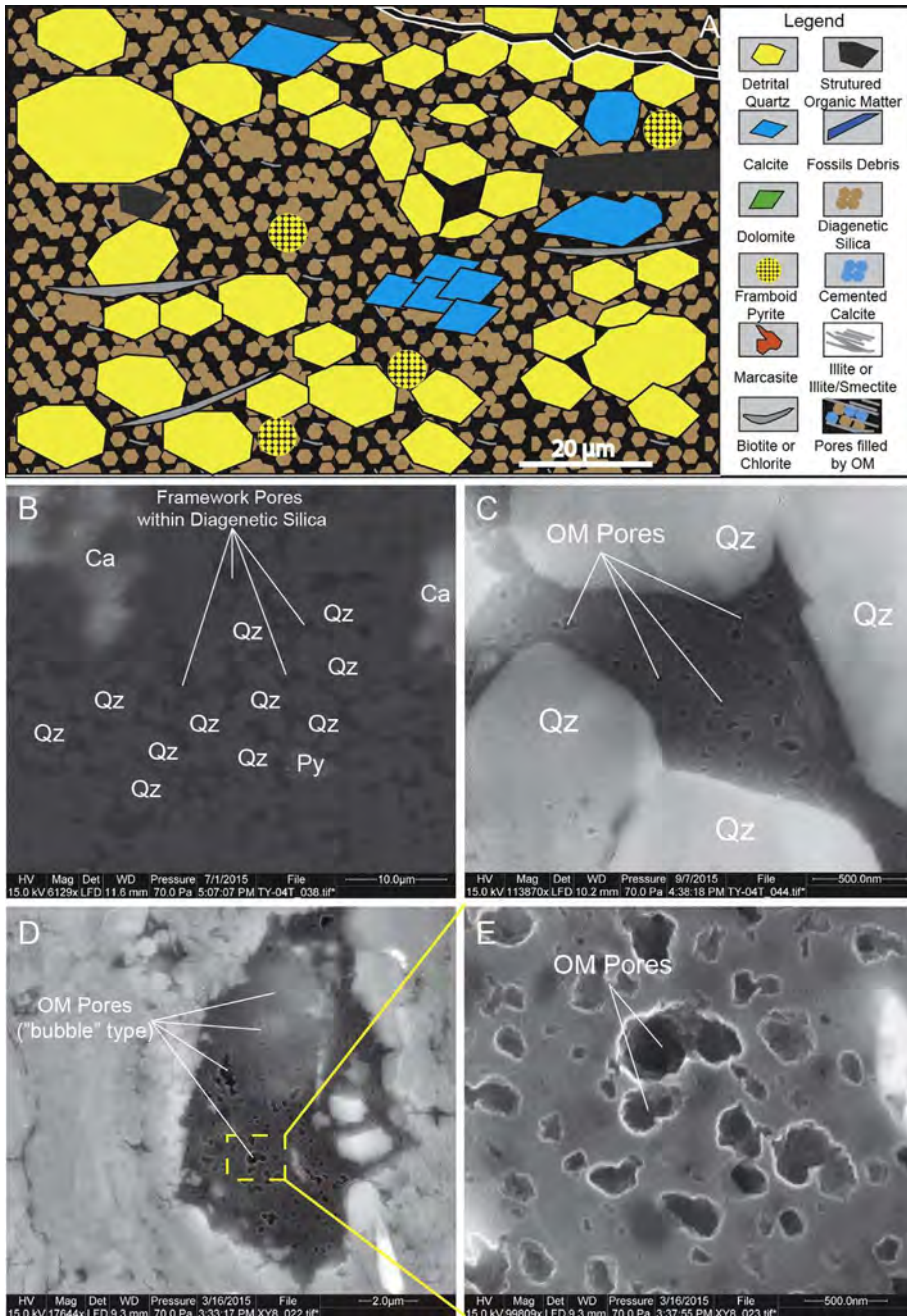


**Fig. 13.** Pore network of black siliceous shales. (A) Generalized schematic diagram of pore network in black siliceous shales. (B) Secondary framework pores within diagenetic silica in black siliceous shales (SE image), Wufeng Formation, Well Tongye-1. (C) Secondary framework pores are filled with amorphous organic matter (Close-up SE image). OM pores are well developed within organic matter. (D) and (E): Bubble pores in amorphous organic matter. OM pores are well connected in organic matter. Qz = quartz; Ca = calcite; Py = pyrite. All the surfaces in SEM images are perpendicular to bedding.

system of gas shale units (Curtis et al., 2011; Loucks et al., 2009; Milliken et al., 2012, 2013; Slatt and O'Brien, 2011). Development of OM pores is mainly controlled by organic matter type, thermal maturation, and total organic matter (TOC). Previous studies suggest that OM pores are well developed in amorphous bitumen, whereas only few OM pores are preserved in structured kerogen (Bernard et al., 2012; Loucks et al., 2009, 2012; Schieber, 2013). In the Devonian New Albany Shale, for instance, no OM pores occur in *Tasmanites* fragments (structured kerogen), irrespective of thermal maturity (Schieber, 2013). In this study, development of OM pores shows similar characteristics in the Wufeng-Longmaxi Formations. OM pores are well developed in and restricted to amorphous organic matter (Fig. 11C, D, E, F). Judging from its habit of infilling pre-existing framework pores this organic matter is interpreted to be bitumen that invaded pore spaces in liquid form. In contrast, *Graptolites* fragments that represent structured kerogen are devoid of OM pores (Fig. 11A and B). In addition, kerogen type also controls development of OM pores. Previous studies show that

OM pores tend to be developed in type I and type II kerogens rather than in type III kerogen (Loucks et al., 2012; Yang et al., 2016). Geochemical analysis of the organic matter in the Wufeng-Longmaxi Formations (Wu et al., 2014) has suggested that kerogen is dominantly type I and type II, and macerals mainly consist of sapropelinite and bituminite, which is favorable for the development of OM pores.

Development of OM pores has been shown to be closely related to the thermal maturity of organic matter (Bernard et al., 2012; Curtis et al., 2012; Loucks and Reed, 2014; Loucks et al., 2009, 2012; Mastalerz et al., 2013; Schieber, 2013). In general, abundant OM pores should only be expected in gas shales whose thermal maturation has reached an  $R_o$  level of approximately 0.6% or higher (the beginning of peak oil generation) (Curtis et al., 2012; Loucks et al., 2009, 2012, 2014; Schieber, 2013). Data from the New Albany Shale (Mastalerz et al., 2013) have shown that the evolution of OM porosity does not follow a linear path with increasing maturity. Primary cracking of organic matter happens at the beginning of the mature stage, resulting in

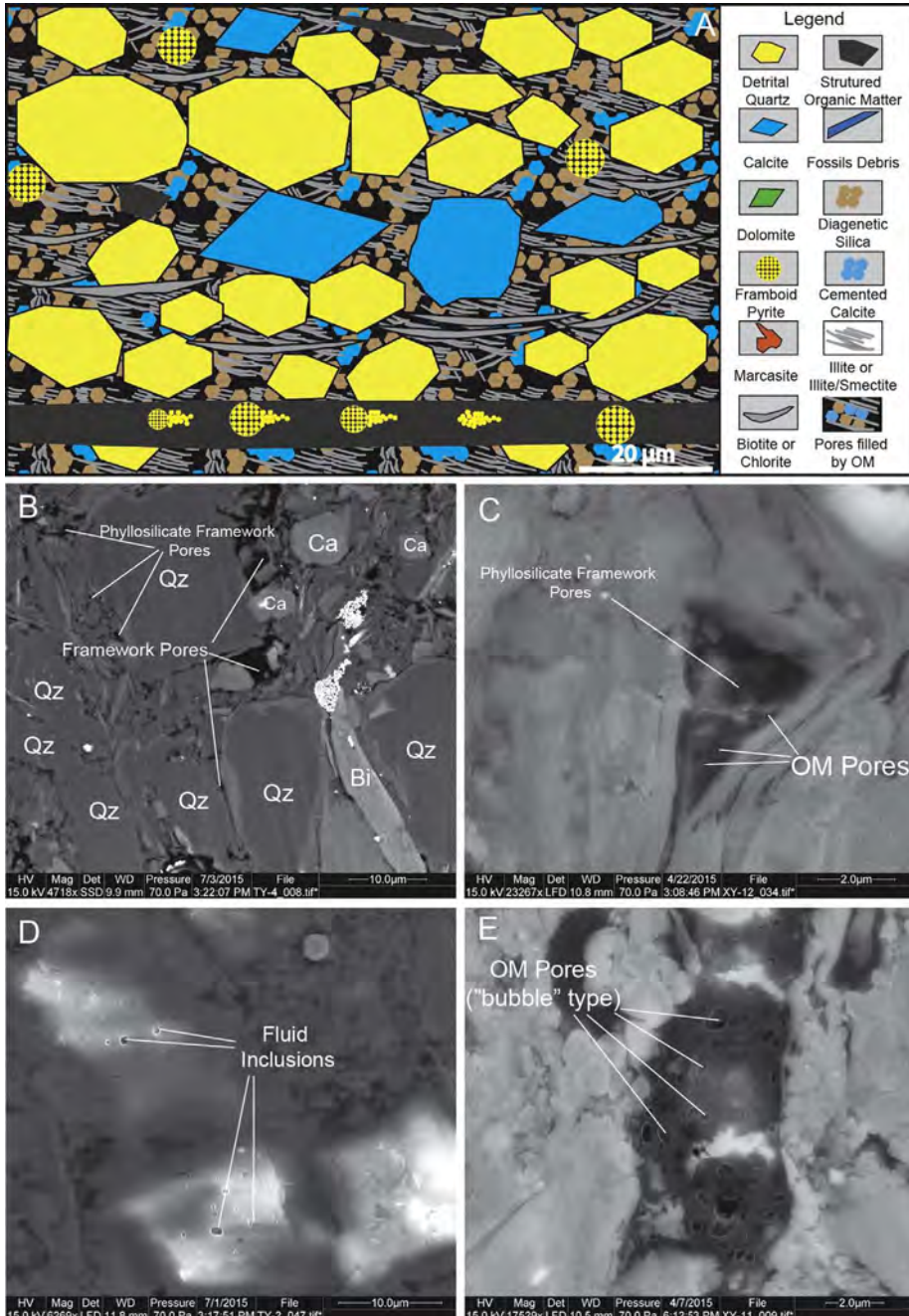


**Fig. 14.** Pore network of black shales. (A) Generalized schematic diagram of pore network in black shales. (B) Primary framework pores and PF pores in black shales (BSE image), Longmaxi Formation, Well Tongye-1. (C) PF pores are filled with amorphous organic matter where OM pores are developed (SE image), Longmaxi Formation, Well Xiyie-1. (D) Fluid inclusions in calcite grains (SE image), Longmaxi Formation, Well Tongye-1. (E) Bubble pores in amorphous organic matter. OM pores are well connected in organic matter. Qz = quartz; Ca = calcite; Py = pyrite. All the surfaces in SEM images were perpendicular to bedding. In images B-E bedding is oriented vertical.

an increase of OM porosity. However, porosity decreases during the late mature stage because previously developed pores are filled by oil or solid bitumen that reduces the available open pore space (Mastalerz et al., 2013). In the postmature stage (> 1.15%), secondary cracking of oil and bitumen to gas can cause secondary development of OM pores, and again increase porosity (Mastalerz et al., 2013). The thermal maturity of the Wufeng-Longmaxi Shales has an average  $R_o$  value of 2.73% (Shi et al., 2015) over large areas, and therefore, the well-developed OM pores within these shale units probably resulted from secondary cracking of organic matter.

In many shale units the abundance of organic matter shows a positive covariation with overall porosity (Chalmers and Bustin, 2008; Loucks et al., 2009; Milliken et al., 2012, 2013; Passey et al., 2010). The point-counting porosity in the Wufeng-Longmaxi Formations shows an overall positive correlation with the TOC values (Fig. 18), although a portion of the overall porosity may not be detected by SEM imaging

(Keller et al., 2011; Milliken and Curtis, 2016; Milliken et al., 2013). In detail, the total porosity of the organic-rich black siliceous shale and black shale (average porosity: 4.96% and 3.41%, respectively) is generally higher than in other organic-poor facies (lower than 2%) (Table 3). Therefore, TOC values appear to correlate positively with total porosity. Milliken et al. (2013) suggested that porosity and pore sizes in OM may decrease with increasing TOC values. In this study, however, porosity in OM does not show a monotonous negative covariation with TOC. OM pores are also well developed in facies with higher TOC contents (Fig. 13C, E). In addition, bubble-type OM pores are more often found in organic-rich facies than in organic-poor facies (Figs. 13E and 14E), which indicates that OM pore sizes in facies with higher TOC tend to be larger than in facies with lower TOC contents. Therefore, it appears that OM porosity and pore sizes are not only controlled by abundance of organic matter, thermal maturity, and organic-matter type, but also by variations in mineralogical composition

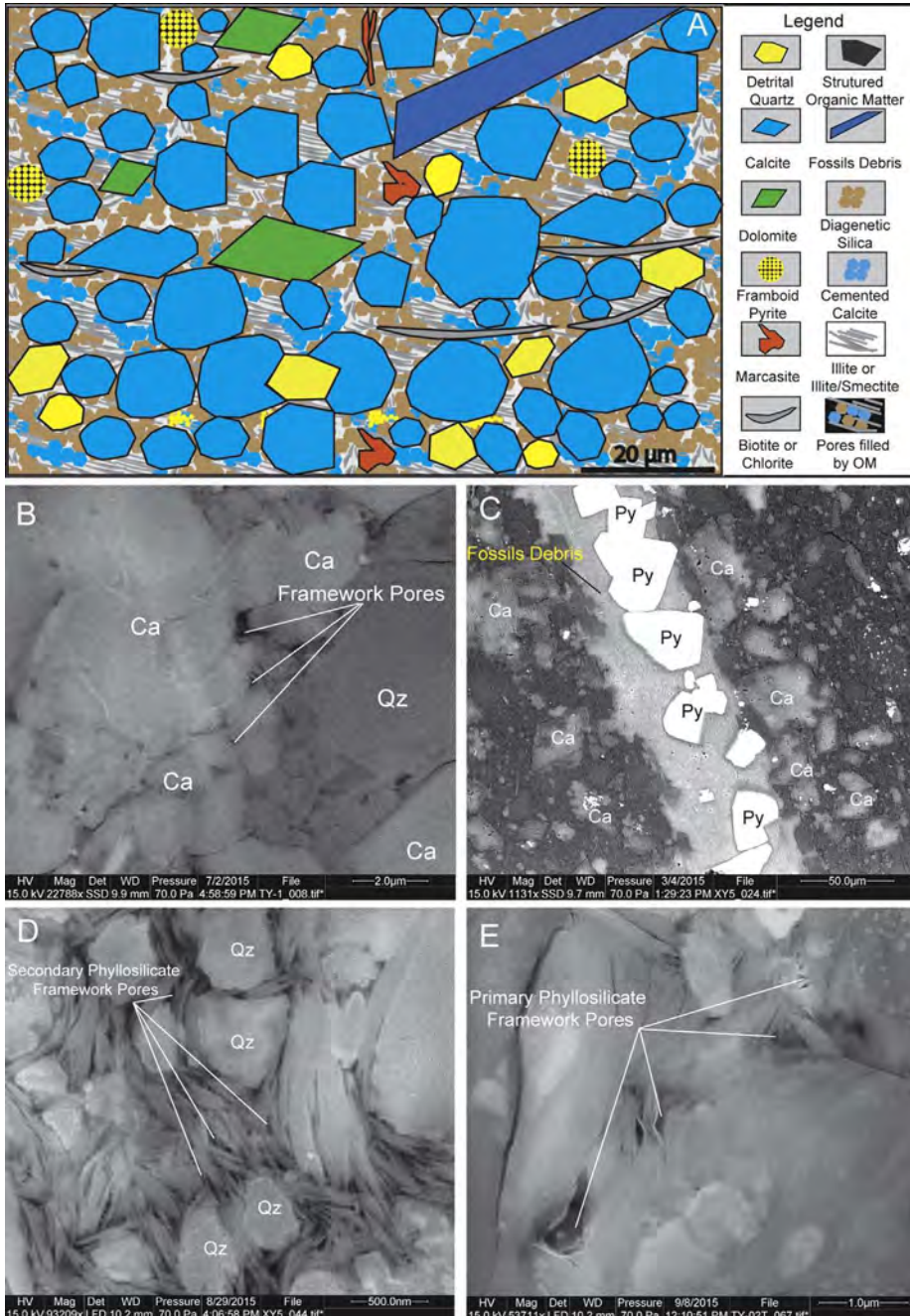


**Fig. 15.** Pore network in muddy fossiliferous shales. (A) Generalized schematic diagram of pore network in muddy fossiliferous facies. (B): Framework pores within calcite grains (BSE image), Guanyinqiao Formation, Well Tongye-1. (C) Calcite grains and fossil debris are disseminated in muddy fossiliferous facies (BSE image), Guanyinqiao Formation, Well Xiye-1. Note partial replacement of calcite shell by pyrite. (D) Secondary PF pores in background matrix. These clay minerals are mixed with diagenetic quartz. Guanyinqiao Formation, Well Xiye-1. (E) Primary PF pores in this facies. Guanyinqiao Formation, Well Tongye-1. Qz = quartz; Ca = calcite; Py = pyrite. All the surfaces in SEM images were perpendicular to bedding. In images B-E bedding is oriented vertical.

and texture that affect preservation of OM pores during the burial and diagenesis. This aspect will be discussed in the following section.

#### 4.6. Pore development through burial diagenesis

Mineral constituents of fine-grain rocks can be classified into three groups on the basis of mechanical and chemical stability: (1) clay minerals (relatively low mechanical and chemical stability), (2) carbonate, feldspar and phosphate (mechanical stable but chemical unstable), and (3) quartz, pyrite and others (relatively high mechanical and chemical stability) (Loucks et al., 2012). These minerals as well as organic matter evolve mechanically or chemically during burial and diagenetic process, significantly affecting pore network system (Figs. 3 and 19). Mechanical compaction is the most significant process for the loss of porosity in shales (Bridge and Demicco, 2008; Loucks et al., 2012; Milliken and Curtis, 2016). During the early history of burial,

framework pores between detrital grains and primary PF pores are mainly lost through mechanical compaction, although some primary PF pores can survive in pressure shadows adjacent to rigid grains (Fig. 10A). However, pore loss in shales through compaction is size-dependent (Milliken and Curtis, 2016). Larger pores are more easily collapsed through compaction, whereas smaller pores (< 100 nm) are especially resistant to mechanical compaction (Day-Stirrat et al., 2012; Dewhurst et al., 1999; Emmanuel and Day-Stirrat, 2012; Milliken and Reed, 2010). Therefore, small framework pores between authigenic silica grains are mostly preserved through compaction (Figs. 7B and 13B). Authigenic silica grains are mostly sourced from dissolution of biogenic opal (i.e., radiolarians) and reprecipitated during early diagenesis (Loucks et al., 2012; Schieber, 2010). Other minerals, including carbonate, phosphate and pyrite, also form during early diagenesis (Loucks et al., 2012; Schieber, 2013), and intrapores within framboidal pyrite form during this time. The diagenetic transformation of smectite

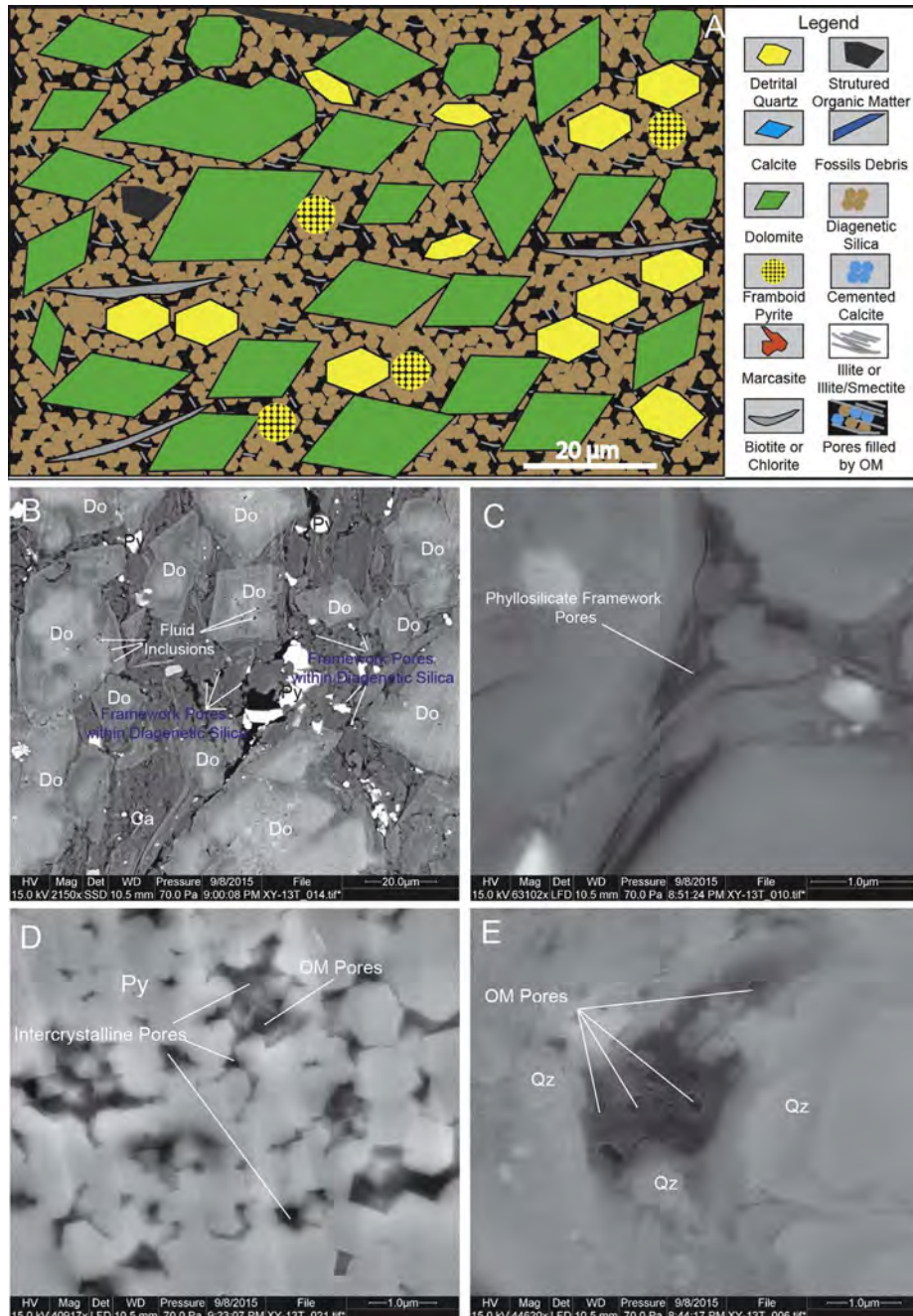


**Fig. 16.** Pore network in black dolomitic siltstone. (A) Generalized schematic diagram of pore network in black dolomitic siltstone. (B) Secondary framework pores and fluid inclusions in black dolomitic siltstone (BSE image), Longmaxi Formation, Well Xiyi-1. (C) Primary PF pores in this facies (SE image), Longmaxi Formation, Well Xiyi-1. (D) Intercrystalline pores within framboidal pyrite, filled with amorphous organic matter (SE image), Longmaxi Formation, Well Xiyi-1. (E) Secondary framework pores within diagenetic quartz are occluded by organic matter in which OM pores are developed (SE image), Longmaxi Formation, Well Xiyi-1Qz = quartz; Ca = calcite; Py = pyrite; Do = dolomite. All the surfaces in SEM images were perpendicular to bedding. In images B-E bedding is oriented vertical.

to illite begins during intermediate burial diagenesis (e.g. Hover et al., 1996; Surdam et al., 1991). During this process, secondary clay minerals as well as related tiny secondary PF pores form (Fig. 10C, D, E, F). Because the associated chemical reactions release dissolved constituents to the pore waters, some new authigenic quartz and carbonate minerals also form (Day-Stirrat et al., 2010; Schieber, 2010) and occlude primary pores as well as forming new framework pores between authigenic minerals. The smectite-to-illite transformation overlaps with the onset of hydrocarbon generation (Loucks et al., 2012; Schieber, 2013), and therefore newly produced oil and bitumen tends to fill prior PF pores and framework pores during migration (e.g. Figs. 13C, 14C and 16E). Decarboxylation of kerogen occurs after the initial stages of smectite transformation, and produces an increase of carboxylic and phenolic acids (MacGowan and Surdam, 1990). These fluid acids induce dissolution of carbonates and feldspars, resulting in formation of dissolution pores associated with these minerals (Fig. 8 A, B).

Pore distribution and pore networks differ from facies to facies, because variable mineralogical composition leads to different burial diagenetic process. For example, bioturbated claystones are dominated by clay minerals. Due to a lack of rigid grains, most of primary PF pores as well as framework pores are lost during mechanical compaction of early burial. Hydrocarbon generation and migration during intermediate burial diagenesis future infills open voids, although this is partially compensated for by development of OM pores in pore filling bitumen (Fig. 12C, E).

In black siliceous shales, for contrast, diagenetic history unfolds differently. Although many primary framework pores between detrital grains collapsed during early burial history, many tiny framework pores between authigenic silica grains that formed during this period resisted mechanical compaction (Fig. 13B). Therefore, a large proportion of void spaces probably remained open after shallow-intermediate burial compaction, and provided enough space to be infilled by amorphous

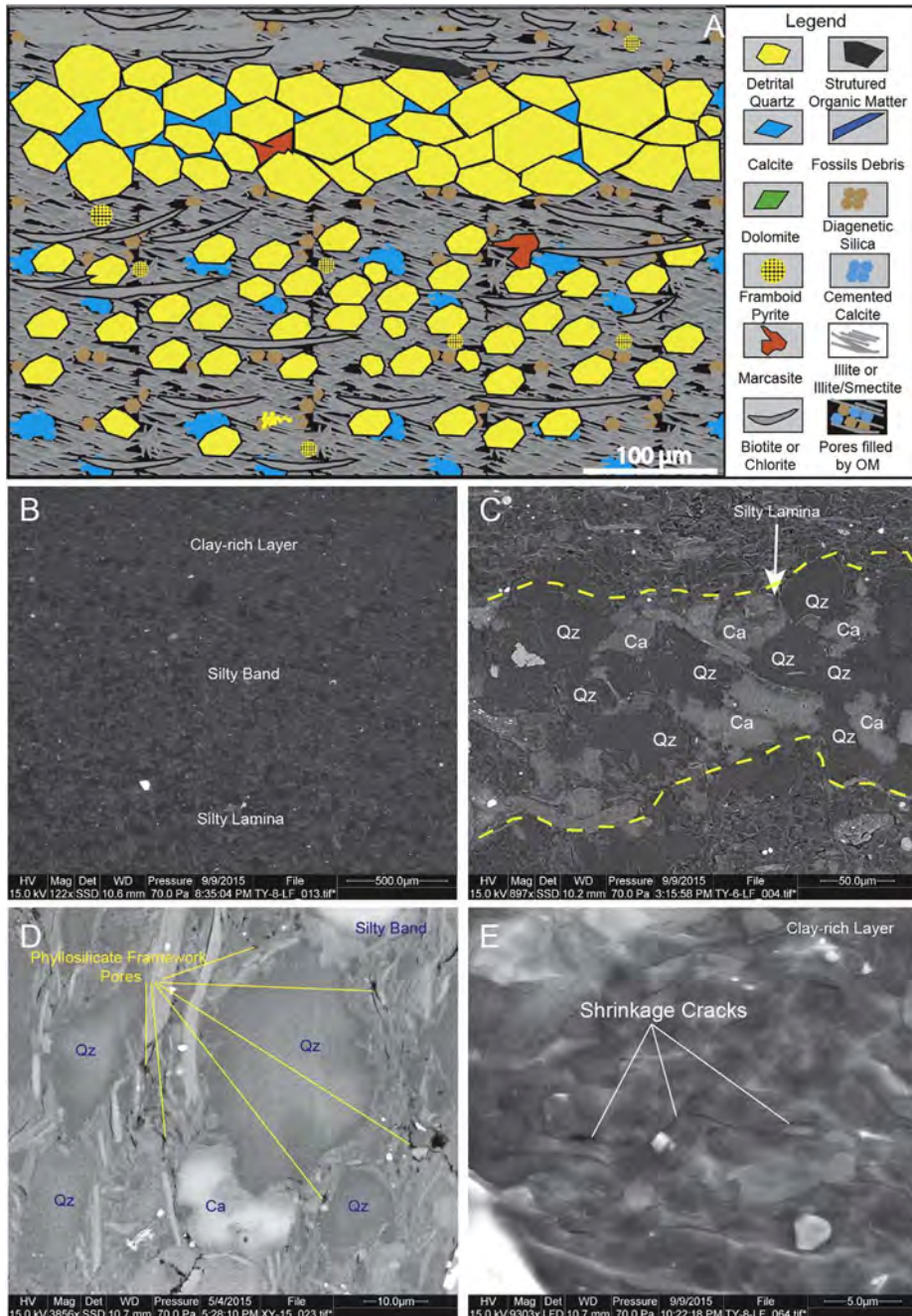


**Fig. 17.** Pore network of muddy siltstones. (A) Generalized schematic diagram of pore network in muddy siltstones. (B) Interbedded layers of clay-rich layer, silty band and silty lamina in muddy siltstones (BSE image), Longmaxi Formation, Well Tongye-1. (C) Silty lamina is strongly compressed and cemented by diagenetic calcite (BSE image). Pores are poorly developed within it. Longmaxi Formation, Well Tongye-1. (D) Admixture of rigid and ductile grains in a silty band (BSE image). Primary PF pores are preserved in it. Longmaxi Formation, Well Xiye-1. (E) Shrinkage cracks in a clay-rich layer (SE image), Longmaxi Formation, Well Tongye-1. Qz = quartz; Ca = calcite.

organic matter (likely bitumen) bitumen during hydrocarbon generation. This assertion is supported by the observed high abundance of amorphous organic matter (average point-counting content is 15.08%) in this facies (Table 3). Most of the amorphous organic matter (bitumen) is protected from compression by rigid mineral (silica) frameworks (Fig. 13C) that prevent collapse of OM pores during compactional gas expulsion (Milliken et al., 2013). This could explain why OM pores are also well developed in the organic-rich facies of the Wufeng–Longmaxi Formations.

Diagenetic processes in the black shales were similar to the black siliceous shales. However, because the black shale facies has a greater proportion of detrital material (silty grains and clay minerals) and less authigenic silica, fewer void spaces were kept open after mechanical compaction. In addition, a somewhat lower content of amorphous organic matter (average point-counting content is 10.37%) (Table 3) puts further limits on OM pore development. In combination, these factors

explain the lower porosity of the black shales (average porosity 3.41%) relative to the black siliceous shales (average porosity 4.96%) (Table 3).

In the muddy fossiliferous shale facies the proportion of carbonate minerals and calcareous fossil debris is high, but most primary PF pores and framework pores between carbonate grains were lost to mechanical and chemical compaction early in diagenesis. Because TOC is very low in this facies only minor carboxylic and phenolic acids are produced by decarboxylation of kerogen and therefore dissolution pores associated with carbonate grains or fossil fragments are poorly developed in the proximal section (well Tongye-1). Consequently, overall porosity is very low (average porosity 1.82%) (Table 3). In the distal area of this facies (well Xiye-1), higher contents of authigenic quartz and TOC lead to preservation of some secondary framework pores (Fig. 15D) and development of OM pores. Therefore, pore development in the distal muddy fossiliferous shale facies is relatively better (average porosity is 2.08%) (Table 3).

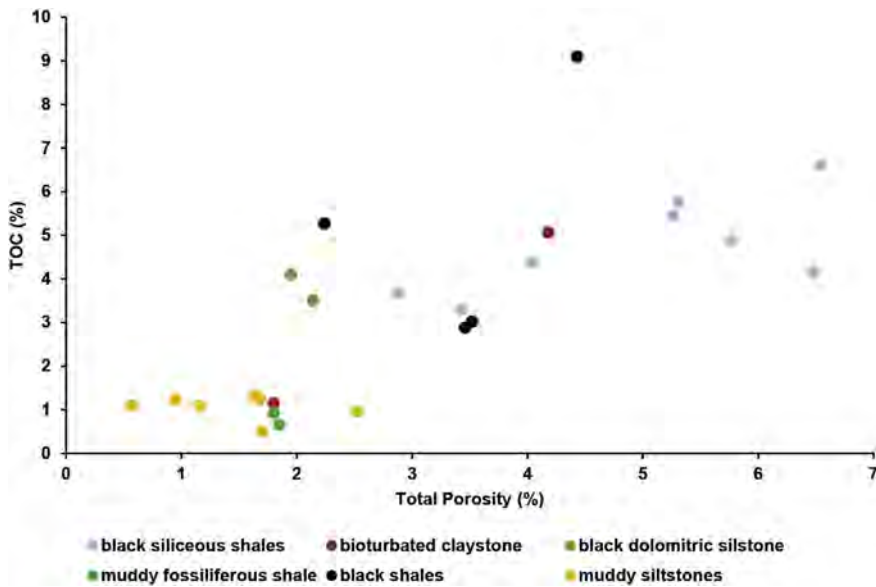


Fig. 18. Plots for total porosity vs. TOC for the different lithofacies of the Wufeng-Longmaxi Formations, northern Guizhou, South China.

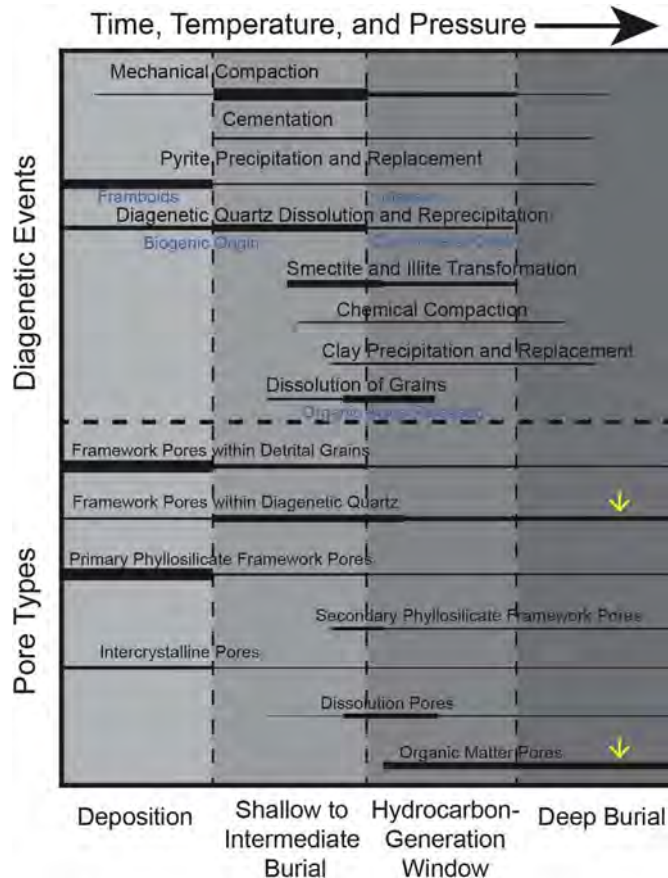


Fig. 19. Parasequence summary diagram of the major stages of burial diagenesis and the relationship of these stages to the evolution of pore types and abundances in the Wufeng-Longmaxi Formations, northern Guizhou, China (Modified after Loucks et al., 2012).

Secondary framework pores between dolomite grains of the black dolomitic siltstone mostly collapsed due to mechanical and chemical compaction in early diagenesis, although a small fraction of framework pores between authigenic quartz grains survived (Fig. 16B). Therefore, void spaces to be filled by amorphous organic matter (bitumen) were limited, a circumstance that is reflected in the relatively small proportion of amorphous organic matter (5%) in this facies (Table 3).

Consequently, the porosity is not as well developed in this facies (average SEM-visible porosity is 1.88%) (Table 3).

In muddy siltstone facies, the heterogeneity of pore networks reflects the variable impact of burial-related processes in different layers. Mechanical compaction during early burial diminished most primary PF pores of clay-rich layers and the framework pores of silty laminae (Fig. 17C, E). In addition, the residual framework pores of the latter were further cemented by calcite (Fig. 17C). As a result, the porosities of clay-rich layers and silty laminae are relatively low (Table 3). In contrast, the porosity of silty bands is high in comparison (up to 2.51%) (Table 3), probably due to preservation of primary PF pores in pressure shadows of silt grains after compaction (Fig. 17D). Some of these void spaces were subsequently filled with bitumen and gained OM pores. Because of the interlayering with low porosity clay-rich layers and silty laminae, the pore networks in this facies are probably poor connected as a whole.

In summary, in spite of variable trajectories of burial diagenesis in all these facies, porosity is mainly controlled by abundance of authigenic silica and TOC. As most of primary PF pores and primary frameworks pores are lost during compaction, porosity is highly dependent on the population of framework pores between authigenic quartz grains. Secondary cracking of amorphous organic matter added porosity after initial infilling of porosity by oil and bitumen migration. Through combination of these two effects, high contents of authigenic quartz and organic matter, pore networks in the black siliceous shales and black shales developed better than in other facies of the that containing and organic matter are apparently better than in other facies of the Wufeng-Longmaxi Formations.

## 5. Conclusions

In this study, seven fine-grained facies are identified in the Wufeng-Longmaxi Formations, namely bioturbated shale, black siliceous shale, muddy fossiliferous shale, black shale, black dolomitic siltstone, gray muddy siltstone, and dark gray muddy siltstone. Accordingly, Framework pores, intrapores, PF pores and OM pores are the four main pore types. Distributions and abundance of these four kinds of pores are significantly variable among different facies, as variable mineralogical composition would lead to different burial diagenetic process. Data from SEM point counts show that the average porosity of the black siliceous shales (4.96%) is highest, whereas the muddy siltstones have the average smallest porosity (1.33%). In these facies, framework pores between detrital and/or carbonate grains are mainly lost through

mechanical compaction, and only a few primary PF pores are preserved in pressure shadows. Notably, distribution of inorganic pores in gray and dark gray muddy siltstones is relatively complex. Generally, clay-rich layers and silty laminae lack pores, whereas silty bands contain primary PF pores. Inorganic pore types of the black siliceous shales as well as the black shale are typified by framework pores between authigenic quartz grains. Unlike framework pores between detrital grains and primary PF pores, the framework pores between authigenic quartz grains are mostly very tiny ( $< 100$  nm) and resist burial compaction. Hence, enrichments of authigenic quartz have a positive impact on overall porosity. Inorganic pores in organic-rich facies are mostly occluded by amorphous organic matter (bitumen) that is dominated by OM pores. Due to favorable kerogen types and high thermal maturity ( $Ro = 2.73\%$ ), OM pores are well developed within amorphous organic matter after primary and secondary cracking. TOC values show a positive covariation with the total SEM visible porosity. In this context, organic matter and authigenic quartz are the dominant controls on porosity.

## Acknowledgments

The research is sponsored by China Postdoctoral Science Foundation funded projects (2017M610958, 2017M620854), National Natural Science Foundation of China (41702124), the Fundamental Research Funds for the Central Universities (2652017292), the and the Indiana University Shale Research Consortium. The authors would like to acknowledge China Scholarship Council for providing student support. Thanks would go to Dr. Zhiye Gao and two anonymous reviewers for their constructive suggestions.

## References

- Afsharpoor, A., Javadpour, F., 2016. Liquid slip flow in a network of shale noncircular nanopores. *Fuel* 180, 580–590.
- Armstrong, H.A., Baldini, J.U.L., Challands, T.J., Grotzke, D.R., Owen, A.W., 2009. Response of the inter-tropical convergence zone to Southern hemisphere cooling during Upper Ordovician glaciation. *Palaeogeogr. Palaeoclimatol. Palaeoecol.* 284, 227–236.
- Bernard, S., Horsfield, B., Schulz, H.-M., Wirth, R., Schreiber, A., Sherwood, N., 2012. Geochemical evolution of organic-rich shales with increasing maturity: a STXM and TEM study of the Posidonia Shale (Lower Toarcian, northern Germany). *Mar. Petroleum Geol.* 31, 70–89.
- Brenchley, P.J., Storch, P., 1989. Environmental-changes in the Hirnantian (Upper Ordovician) of the Prague Basin, Czechoslovakia. *Geol. J.* 24, 165–181.
- Bridge, J., Demicco, R., 2008. *Earth Surface Processes, Landforms and Sediment Deposits*. Cambridge University Press.
- Chalmers, G.R., Bustin, R.M., 2008. Lower Cretaceous gas shales in northeastern British Columbia, Part II: evaluation of regional potential gas resources. *Bull. Can. Petroleum Geol.* 56, 22–61.
- Chen, S., Xia, X., Fu, C., 2013a. Classification of pore structures in shale gas reservoir at the Longmaxi Formation in the south of Sichuan Basin. *J. China Coal Soc.* 38, 760–765.
- Chen, S., Xia, X., Qin, Y., Fu, C., Hu, L., 2013b. Classification of pore structures in shale gas reservoir at the Longmaxi Formation in the south of Sichuan Basin. *J. China Coal Soc.* 38, 760–765.
- Chen, S., Zhu, Y., Wang, H., Liu, H., Wei, W., Fang, J., 2011. Shale gas reservoir characterisation: a typical case in the southern Sichuan Basin of China. *Energy* 36, 6609–6616.
- Chen, X., Fan, J.X., Wang, W.H., Wang, H.Y., Nie, H.K., Shi, X.W., Wen, Z.D., Chen, D.Y., Li, W.J., 2017. Stage-progressive distribution pattern of the Lungmachi black graphitic shales from Guizhou to Chongqing, Central China. *Sci. China Earth Sci.* 60, 1133–1146.
- Chen, X., Rong, J., Li, Y., Boucot, A.J., 2004. Facies patterns and geography of the Yangtze region, South China, through the Ordovician and Silurian transition. *Palaeogeogr. Palaeoclimatol. Palaeoecol.* 204, 353–372.
- Chen, X., Xiao, C., Chen, H.y., 1987. Wufengian (Ashgillian) graptolite faunal differentiation and anoxic environment in South China. *Acta Palaeontol. Sin.* 26, 326–344.
- Curtis, M.E., Ambrose, R.J., Sondergeld, C.H., 2010. Structural Characterization of Gas Shales on the Micro-and Nano-scales, Canadian Unconventional Resources and International Petroleum Conference. Society of Petroleum Engineers.
- Curtis, M.E., Ambrose, R.J., Sondergeld, C.H., Rai, C.S., 2011. Investigation of the Relationship between Organic Porosity and Thermal Maturity in the Marcellus Shale, North American Unconventional Gas Conference and Exhibition. Society of Petroleum Engineers.
- Curtis, M.E., Cardott, B.J., Sondergeld, C.H., Rai, C.S., 2012. Development of organic porosity in the Woodford Shale with increasing thermal maturity. *Int. J. Coal Geol.* 103, 26–31.
- Dai, J., Zou, C., Liao, S., Dong, D., Ni, Y., Huang, J., Wu, W., Gong, D., Huang, S., Hu, G., 2014. Geochemistry of the extremely high thermal maturity Longmaxi shale gas, southern Sichuan Basin. *Org. Geochem.* 74, 3–12.
- Day-Stirrat, R.J., Dutton, S.P., Milliken, K.L., Loucks, R.G., Aplin, A.C., Hillier, S., van der Pluijm, B.A., 2010. Fabric anisotropy induced by primary depositional variations in the silt: clay ratio in two fine-grained slope fan complexes: Texas Gulf Coast and northern North Sea. *Sediment. Geol.* 226, 42–53.
- Day-Stirrat, R.J., Flemings, P.B., You, Y., Aplin, A.C., van der Pluijm, B.A., 2012. The fabric of consolidation in Gulf of Mexico mudstones. *Mar. Geol.* 295–298, 77–85.
- Desbois, G., Urai, J., Kukla, P., 2009. Morphology of the pore space in claystones—evidence from BIB/FIB ion beam sectioning and cryo-SEM observations. *Earth Discuss.* 4, 1–19.
- Dewhurst, D.N., Aplin, A.C., Sarda, J.P., 1999. Influence of clay fraction on pore-scale properties and hydraulic conductivity of experimentally compacted mudstones. *J. Geophys. Res. Solid Earth* 104, 29261–29274.
- Emmanuel, S., Day-Stirrat, R.J., 2012. A framework for quantifying size dependent deformation of nano-scale pores in mudrocks. *J. Appl. Geophys.* 86, 29–35.
- Fortey, R.A., Cocks, L.R.M., 2005. Late Ordovician global warming - The Boda event. *Geology* 33, 405–408.
- Götze, J., Zimmerle, W., 2000. Quartz and Silica as Guide to Provenance in Sediments and Sedimentary Rocks.
- Guo, S., Guo, J., Liu, C., Zhang, L., Guo, X., Xiao, P., 2016. Shale Gas Accumulation Potential of Lower Silurian Longmaxi Formation in Northern Guizhou. *Journal of Central South University (Science and Technology)* 47, pp. 1973–1980.
- Guo, T., Zhang, H., 2014. Formation and enrichment mode of Jiaoshiba shale gas field, Sichuan Basin. *Petroleum Explor. Dev.* 41, 31–40.
- Guo, X., Hu, D., Li, Y., Liu, R., Wang, Q., 2014a. Geological features and reservoir mode of shale gas reservoirs in Longmaxi Formation of the Jiaoshiba area. *Acta Geol. Sinica-English Ed.* 88, 1811–1821.
- Guo, X., Li, Y., Liu, R., Wang, Q., 2014b. Characteristics and controlling factors of micro-pore structures of the Longmaxi shale in the Jiaoshiba area, Sichuan Basin. *Nat. Gas. Ind. B* 1, 165–171.
- Guy Plint, A., Baas, J., 2014. Mud dispersal across a Cretaceous prodelta: Storm-generated, wave-enhanced sediment gravity flows inferred from mudstone microtexture and microfacies. *Sedimentology* 61, 609–647.
- Harazim, D., McIlroy, D., 2015. Mud-rich density-driven flows along an early Ordovician Storm-dominated Shoreline: implications for shallow-marine facies models. *J. Sediment. Res.* 85, 509–528.
- Hayes, J.B., 1991. Porosity evolution of sandstones related to vitrinite reflectance. *Org. Geochem.* 17, 117–129.
- Hover, V.C., Peacor, D.R., Walter, L.M., 1996. STEM/AEM evidence for preservation of burial diagenetic fabrics in Devonian shales: implications for fluid/rock interaction in cratonic basins (USA). *J. Sediment. Res.* 66.
- Javadpour, F., 2009. Nanopores and apparent permeability of gas flow in mudrocks (shales and siltstone). *J. Can. Petroleum Technol.* 48, 16–21.
- Jiang, Z., Guo, L., Liang, C., Wang, Y., Liu, M., 2013. Lithofacies and sedimentary characteristics of the Silurian Longmaxi shale in the southeastern Sichuan Basin, China. *J. Palaeogeogr.* 2, 238–251.
- Jiao, K., Yao, S., Liu, C., Gao, Y., Wu, H., Li, M., Tang, Z., 2014. The characterization and quantitative analysis of nanopores in unconventional gas reservoirs utilizing FESEM-FIB and image processing: an example from the lower Silurian Longmaxi Shale, upper Yangtze region, China. *Int. J. Coal Geol.* 128–129, 1–11.
- Keller, L.M., Holzer, L., Wepf, R., Gasser, P., Münch, B., Marschall, P., 2011. On the application of focused ion beam nanotomography in characterizing the 3D pore space geometry of Opalinus clay. *Phys. Chem. Earth, Parts A/B/C* 36, 1539–1544.
- Ko, L.T., Loucks, R.G., Ruppel, S.C., Zhang, T., Peng, S., 2017. Origin and characterization of Eagle Ford pore networks in the south Texas Upper Cretaceous shelf. *Aapg Bull.* 101, 387–418.
- Land, L., Milliken, K., 2009. Special Publication. Regional Loss of SiO<sub>2</sub> and CaCO<sub>3</sub>, and Gain of K<sub>2</sub>O during Burial Diagenesis of Gulf Coast Mudrocks, USA. *Quartz Cementation in Sandstones*, vol 29, pp. 183–197.
- Lazar, O.R., Bohacs, K.M., Macquaker, J.H.S., Schieber, J., Demko, T.M., 2015. Capturing key attributes of fine-grained sedimentary rocks in outcrops, cores, and thin sections: nomenclature and description guidelines. *J. Sediment. Res.*, vol. 85, 230–246.
- Li, X., Wang, Z., Guo, M., Zhang, J., Qi, S., Zhou, B., Zhang, W., 2016. Pore Structure Characteristics of the Lower Paleozoic Formation Shale Gas Reservoir in Northern Guizhou. *Journal of China University of Mining & Technology* 45, pp. 1172–1183.
- Li, Y., Schieber, J., Fan, T., Li, Z., Zhang, J., 2017. Regional depositional changes and their controls on carbon and sulfur cycling across the Ordovician-Silurian boundary, northwestern Guizhou, South China. *Palaeogeogr. Palaeoclimatol. Palaeoecol.* 485, 816–832.
- Liang, C., Jiang, Z., Zhang, C., Guo, L., Yang, Y., Li, J., 2014. The shale characteristics and shale gas exploration prospects of the Lower Silurian Longmaxi shale, Sichuan Basin, South China. *J. Nat. Gas Sci. Eng.* 21, 636–648.
- Loucks, R.G., Reed, R.M., 2014. Scanning-electron-microscope Petrographic Evidence for Distinguishing Organic-matter Pores Associated with Depositional Organic Matter versus Migrated Organic Matter in Mudrock.
- Loucks, R.G., Reed, R.M., Ruppel, S.C., Hammes, U., 2012. Spectrum of pore types and networks in mudrocks and a descriptive classification for matrix-related mudrock pores. *Aapg Bull.* 96, 1071–1098.
- Loucks, R.G., Reed, R.M., Ruppel, S.C., Jarvie, D.M., 2009. Morphology, genesis, and distribution of nanometer-scale pores in siliceous mudstones of the mississippian barnett shale. *J. Sediment. Res.* 79, 848–861.
- MacGowan, D.B., Surdam, R.C., 1990. Carboxylic acid anions in formation waters, San Joaquin basin and Louisiana Gulf coast, USA—implications for clastic diagenesis.

- Appl. Geochem. 5, 687–701.
- Macquaker, J.H.S., Taylor, K.G., Gawthorpe, R.L., 2007. High-resolution facies analyses of mudstones: implications for paleoenvironmental and sequence stratigraphic interpretations of Offshore ancient mud-dominated successions. *J. Sediment. Res.* 77, 324–339.
- Mastalerz, M., Schimmelmann, A., Drobniak, A., Chen, Y., 2013. Porosity of Devonian and Mississippian New Albany Shale across a maturation gradient: insights from organic petrology, gas adsorption, and mercury intrusion. *Aapg Bull.* 97, 1621–1643.
- Melchin, M.J., Mitchell, C.E., Holmden, C., Storch, P., 2013. Environmental changes in the Late Ordovician-early Silurian: review and new insights from black shales and nitrogen isotopes. *Geol. Soc. Am. Bull.* 125, 1635–1670.
- Metcalfe, I., 1994. Late palaeozoic and mesozoic palaeogeography of eastern Pangea and Tethys. In: Embry, A.F., Beauchamp, B., Glass, D.J. (Eds.), *Pangea: Global Environments and Resources*. Canadian Society of Petroleum Geologists, pp. 97–111.
- Metcalfe, I., 2013. Gondwana dispersion and Asian accretion: tectonic and palaeogeographic evolution of eastern Tethys. *J. Asian Earth Sci.* 66, 1–33.
- Milliken, K.L., Curtis, M.E., 2016. Imaging pores in sedimentary rocks: Foundation of porosity prediction. *Mar. Petroleum Geol.* 73, 590–608.
- Milliken, K.L., Esch, W.L., Reed, R.M., Zhang, T.W., 2012. Grain assemblages and strong diagenetic overprinting in siliceous mudrocks, barnett shale (mississippian), Fort Worth basin, Texas. *Aapg Bull.* 96, 1553–1578.
- Milliken, K.L., Reed, R.M., 2010. Multiple causes of diagenetic fabric anisotropy in weakly consolidated mud, Nankai accretionary prism, IODP Expedition 316. *J. Struct. Geol.* 32, 1887–1898.
- Milliken, K.L., Rudnicki, M., Awwiller, D.N., Zhang, T., 2013. Organic matter-hosted pore system, marcellus formation (devonian), Pennsylvania. *Aapg Bull.* 97, 177–200.
- Milner, M., McLin, R., Petriello, J., 2010. Imaging texture and porosity in mudstones and shales: comparison of secondary and ion-milled backscatter SEM methods. In: *Canadian Unconventional Resources and International Petroleum Conference*. Society of Petroleum Engineers.
- Mitchell, C.E., Storch, P., Holmden, C., Melchin, M.J., Gutiérrez-Marco, J.C., 2011. New stable isotope data and fossils from the Hirnantian Stage in Bohemia and Spain: implications for correlation and paleoclimate. In: Gutiérrez-Marco, J.C., Rábano, I., García-Bellido, D. (Eds.), *Ordovician of the World: Cuadernos del Museo Geominero. Instituto Geológico y Minero de España*, Madrid, Spain.
- Moreau, J., 2011. The late Ordovician deglaciation sequence of the sw Murzuq basin (Libya). *Basin Res.* 23, 449–477.
- Mou, C., Ge, X., Xu, X., Zhou, K., Liang, W., Wang, X., 2014. Lithofacies palaeogeography of the late Ordovician and its petroleum geological significance in middle-upper Yangtze region. *J. Palaeogeogr. Chin.* Ed. 16, 427–440.
- Passey, Q.R., Bohacs, K., Esch, W.L., Klimentidis, R., Sinha, S., 2010. From Oil-prone Source Rock to Gas-producing Shale Reservoir-geologic and Petrophysical Characterization of Unconventional Shale Gas Reservoirs, International Oil and Gas Conference and Exhibition in China. Society of Petroleum Engineers.
- Qin, C., Yu, Q., Liu, W., Yan, J., Zhang, H., 2017. Reservoir characteristics and exploration prospect of organic-rich mudstone, Longmaxi Formation in northern Guizhou. *J. Northeast Petroleum Univ.* 39, 13–24.
- Ran, B., Liu, S., Sun, W., Ye, Y., Qiu, J., Zhang, J., Yang, D., 2016. Lithofacies classification of shales of the lower paleozoic Wufeng-Longmaxi formations in the Sichuan Basin and its surrounding areas, China. *Earth Sci. Front.* 23, 96–107.
- Rong, J., Chen, X., 1987. Faunal differentiation, biofacies and lithofacies pattern of late Ordovician (Ashgillian) in South China. *Acta Palaeontol. Sin.* 26, 507–535.
- Schieber, J., 1999. Distribution and deposition of mudstone facies in the upper devonian Sonyea group of New York. *J. Sediment. Res.* 69, 909–925.
- Schieber, J., Krinsley, D., Ricciuti, L., 2000. Diagenetic origin of quartz silt in mudstones and implications for silica cycling. *Nature* 406, 981–985.
- Schieber, J., 2010. Common themes in the formation and preservation of intrinsic porosity in shales and mudstones-illustrated with examples across the Phanerozoic. In: *SPI Unconventional Gas Conference*. Society of Petroleum Engineers.
- Schieber, J., 2011. Iron Sulfide formation. In: Reitner, J., Thiel, V. (Eds.), *Encyclopedia of Geobiology*. Springer Netherlands, Dordrecht, pp. 486–502.
- Schieber, J., 2013. SEM Observations on Ion-milled Samples of Devonian Black Shales from Indiana and New York: the Petrographic Context of Multiple Pore Types.
- Schieber, J., Lazar, R., Bohacs, K., Klimentidis, R., Dumitrescu, M., Ottmann, J., 2016. An SEM Study of Porosity in the Eagle Ford Shale of Texas—Pore Types and Porosity Distribution in Depositional and Sequence-stratigraphic Context. pp. 167–186.
- Schönlau, H.P., Ferretti, A., Gaggero, L., Hammarlund, E., Harper, D.A.T., Histon, K., Prialowder, H., Spötl, C., Storch, P., 2011. The late Ordovician glacial event in the Carnic Alps (Austria). In: Gutiérrez-Marco, J.C., Rábano, I., García-Bellido, D. (Eds.), *Ordovician of the World: Cuadernos del Museo Geominero. Instituto Geológico y Minero de España*, Madrid, Spain, pp. 515–526.
- Shi, M., Yu, B., Xue, Z., Wu, J., Yuan, Y., 2015. Pore characteristics of organic-rich shales with high thermal maturity: a case study of the Longmaxi gas shale reservoirs from well Yuye-1 in southeastern Chongqing, China. *J. Nat. Gas Sci. Eng.* 26, 948–959.
- Slatt, R.M., O'Brien, N.R., 2011. Pore types in the Barnett and Woodford gas shales: contribution to understanding gas storage and migration pathways in fine-grained rocks. *Aapg Bull.* 95, 2017–2030.
- Su, W., Huff, W.D., Ettensohn, F.R., Liu, X., Zhang, J.e, Li, Z., 2009. K-bentonite, black-shale and flysch successions at the Ordovician–Silurian transition, South China: possible sedimentary responses to the accretion of Cathaysia to the Yangtze Block and its implications for the evolution of Gondwana. *Gondwana Res.* 15, 111–130.
- Surdam, R.C., MacGowan, D.B., Dunn, T.L., 1991. Predictive models for sandstone diagenesis. *Org. Geochem.* 17, 243–253.
- Tang, X., Jiang, Z., Li, Z., Gao, Z., Bai, Y., Zhao, S., Feng, J., 2015. The effect of the variation in material composition on the heterogeneous pore structure of high-maturity shale of the Silurian Longmaxi formation in the southeastern Sichuan Basin, China. *J. Nat. Gas Sci. Eng.* 23, 464–473.
- Taylor, A., Goldring, R., 1993. Description and analysis of bioturbation and ichnofabric. *J. Geol. Soc.* 150, 141–148.
- Taylor, K.G., Macquaker, J.H.S., 2000. Early diagenetic pyrite morphology in a mudstone-dominated succession: the lower jurassic cleveland ironstone formation, eastern England. *Sediment. Geol.* 131, 77–86.
- Tian, H., Pan, L., Xiao, X., Wilkins, R.W., Meng, Z., Huang, B., 2013. A preliminary study on the pore characterization of Lower Silurian black shales in the Chuandong Thrust Fold Belt, southwestern China using low pressure N 2 adsorption and FE-SEM methods. *Mar. Petroleum Geol.* 48, 8–19.
- Wang, F., Guan, J., Feng, W., Bao, L., 2013. Evolution of overmature marine shale porosity and implication to the free gas volume. *Petroleum Explor. Dev.* 40, 819–824.
- Wang, P., Jiang, Z., Ji, W., Zhang, C., Yuan, Y., Chen, L., Yin, L., 2016a. Heterogeneity of intergranular, intraparticle and organic pores in Longmaxi shale in Sichuan Basin, South China: evidence from SEM digital images and fractal and multifractal geometries. *Mar. Petroleum Geol.* 72, 122–138.
- Wang, Y., Dong, D., Yang, H., He, L., Wang, S., Huang, J., Pu, B., Wang, S., 2014. Quantitative characterization of reservoir space in the lower Silurian Longmaxi shale, southern Sichuan, China. *Sci. China Earth Sci.* 57, 313–322.
- Wang, Y., Wang, H., Zhang, C., Li, X., Dong, D., 2017. Fracture pore evaluation of the upper Ordovician Wufeng to lower Silurian Longmaxi formations in southern Sichuan Basin, SW China. *Petroleum Explor. Dev.* 44, 563–572.
- Wang, Y., Wang, S., Dong, D., 2016b. Lithofacies characterization of Longmaxi Formation of the lower Silurian, southern Sichuan. *Earth Sci. Front.* 23, 119–133.
- Wilson, R.D., 2012. Facies Analysis and Sequence Stratigraphy of the Middle Devonian (Givetian) Geneseo Formation of New York: Implications for Accommodation During a Eustatic Sea-Level Rise. Indiana University.
- Wilson, R.D., Schieber, J., 2014. Muddy prodeltaic hyperpycnites in the lower genesee group of Central New York, USA: implications for mud transport in epicontinental seas. *J. Sediment. Res.* 84, 866–874.
- Wilson, R.D., Schieber, J., 2015. Sedimentary facies and depositional environment of the Middle devonian geneseo formation of New York, U.S.A. *J. Sediment. Res.* 85, 1393–1415.
- Wilson, R.D., Schieber, J., 2016. The influence of primary and secondary sedimentary features on reservoir quality: examples from the geneseo formation of New York, U.S.A. In: Olson, T. (Ed.), *Imaging Unconventional Reservoir Pore Systems*, pp. 167–184.
- Wu, Y., Fan, T., Zhang, J., Jiang, S., Li, Y., Zhang, J., Xie, C., 2014. Characterization of the upper Ordovician and lower Silurian marine shale in northwestern Guizhou Province of the upper Yangtze block, South China: implication for shale gas potential. *Energ. Fuel* 28, 3679–3687.
- Yan, D., Chen, D., Wang, Q., Wang, J., 2012. Predominance of stratified anoxic Yangtze Sea interrupted by short-term oxygenation during the Ordo-Silurian transition. *Chem. Geol.* 291, 69–78.
- Yang, F., Ning, Z., Liu, H., 2014. Fractal characteristics of shales from a shale gas reservoir in the Sichuan Basin, China. *Fuel* 115, 378–384.
- Yang, R., He, S., Yi, J., Hu, Q., 2016. Nano-scale pore structure and fractal dimension of organic-rich Wufeng-Longmaxi shale from Jiaoshiba area, Sichuan Basin: investigations using FE-SEM, gas adsorption and helium pycnometry. *Mar. Petroleum Geol.* 70, 27–45.
- Zheng, H., Gao, B., Peng, Y., Nie, H., Yang, F., 2013. Sedimentary evolution and shale gas exploration direction of the Lower Silurian in Middle-Upper Yangtze area. *J. Palaeogeogr. Chin.* Ed. 15, 645–656.
- Zhang, L., Fan, J., Chen, Q., 2014. Reconstruction of the mid-Hirnantian palaeotopography in the Upper Yangtze region, South China. *Est. J. Earth Sci.* 63 (4), 329.
- Zhang, L.N., Fan, J.X., Chen, Q., 2016. Geographic distribution and palaeogeographic reconstruction of the Upper Ordovician Kuanyinchiao Bed in South China (in Chinese). *Chin. Sci. Bull.* 61, 2053–2063. <https://doi.org/10.1360/N972015-00981>.
- Zinkernagel, U., 1978. *Cathodoluminescence of Quartz and its Application to Sandstone Petrology*.